Inferring and validating mechanistic models of neural microcircuits based on spike-train data

Josef Ladenbauer[1,2,3], Sam McKenzie[4], Daniel Fine English[4,5], Olivier Hagens[6] and Srdjan Ostojic[3]

[1] Department of Software Engineering and Theoretical Computer Science, Technische Universität Berlin, Berlin, Germany
[2] Bernstein Center for Computational Neuroscience Berlin, Berlin, Germany
[3] Laboratoire de Neurosciences Cognitives, INSERM U960, École Normale Supérieure - PSL Research University, Paris, France
[4] Neuroscience Institute, New York University, New York, NY, USA
[5] School of Neuroscience, Virginia Tech, Blacksburg, VA, USA
[6] Laboratory of Neural Microcircuitry (LNMC), Brain Mind Institute, School of Life Sciences, École Polytechnique Fédérale de Lausanne, Lausanne, Switzerland

Abstract

The interpretation of neuronal spike train recordings often relies on abstract statistical models that allow for principled parameter estimation and model selection but provide only limited insights into underlying microcircuits. In contrast, mechanistic models are useful to interpret microcircuit dynamics, but are rarely quantitatively matched to experimental data due to methodological challenges. Here we present analytical methods to efficiently fit spiking circuit models to single-trial spike trains. Using the maximal-likelihood approach, we statistically infer the mean and variance of hidden inputs, neuronal adaptation properties and connectivity for coupled integrate-and-fire neurons. Evaluations based on simulated data, and validations using ground truth recordings in vitro and in vivo demonstrated that parameter estimation is very accurate, even for highly sub-sampled networks. We finally apply our methods to recordings from cortical neurons of awake ferrets and reveal population-level equalization between hidden excitatory and inhibitory inputs. The methods introduced here enable a quantitative, mechanistic interpretation of recorded neuronal population activity.

Introduction

In recent years neuronal spike train data have been collected at an increasing pace, with the ultimate aim of unraveling how neural circuitry implements computations that underlie behavior. Often these data are acquired from extracellular electrophysiological recordings in vivo without knowledge of neuronal input and connections between neurons. To interpret such data, the recorded spike trains are frequently analyzed by fitting parametric phenomenological models that describe statistical dependencies in the data. A typical example consists in fitting generalized linear models to characterize the mapping between measured (sensory) input and neuronal spiking activity [1–5]. These approaches are very useful for quantifying the structure in the data, and benefit from statistically principled parameter estimation and model selection methods. However, their interpretative power is limited as the underlying models typically do not incorporate prior biophysical constraints, and therefore have a limited capacity for identifying circuit mechanisms.

Mechanistic models of coupled neurons on the other hand involve interpretable variables and parameters, and have proven essential for analyzing neural circuits. A prominent class of models for this purpose are spiking neuron models of the integrate-and-fire (I&F) type. Models of this class implement in a simplified manner the key biophysical constraints and can reproduce and predict neuronal activity with a remarkable degree of accuracy [6–8], essentially matching the performance of biophysically detailed models with many parameters [9, 10]; thus, they have become state-of-the-art models for describing neural activity in in-vivo like conditions [7, 11, 12]. In particular, they have been applied in a multitude of studies on local circuits [13–19],

network dynamics [20–24] as well as in neuromorphic hardware systems [25–27]. I&F neurons can be fit in straightforward ways to membrane voltage recordings with knowledge of the neuronal input, typically from in-vitro preparations [7, 9, 11, 12, 28–30]. Having only access to the spike times as in a typical in-vivo setting however poses a substantial challenge for the estimation of parameters. Estimation methods that rely on numerical simulations to maximize a likelihood or minimize a cost function [31–33] strongly suffer from the presence of intrinsic variability (noise) in this case. Consequently, qualitatively comparing the model output with experimental data is typically the only validation of mechanistic spiking circuit models.

To date, model selection methods based on extracellular recordings are thus much more advanced and principled for statistical/phenomenological models than for mechanistic circuit models. To bridge this methodological gap, here we present analytical tools to efficiently fit I&F circuits to observed spike times from a single trial. By maximizing analytically computed likelihood functions, we infer the statistics of hidden inputs, neuronal adaptation properties and synaptic coupling strengths, and evaluate our approach extensively using simulated data. Importantly, we validate our inference methods for these three features using in-vitro and in-vivo ground truth data from whole-cell [34] and combined juxtacellular-extracellular recordings [35]. We finally apply the methods to extracellular recordings from primary auditory cortex of awake behaving ferrets, in particular, assessing the hidden neuronal inputs based on single-unit spike times.

Our work demonstrates that neuronal and network properties can be accurately and efficiently estimated from spike trains using biophysically constrained I&F models, and indicates the potential of this approach for the inference of microcircuit models from extracellular recordings. Numerical implementations for our methods are provided under a free license as an open source project.

Results

Our results are structured as follows. We outline our methods in section 1 and evaluate them in the subsequent sections using both simulated data and ground truth recordings: for statistical inference of fluctuating background input in section 2, input perturbations in section 3, synaptic coupling in section 4, and neuronal adaptation in section 5. In section 6 we then apply our methods to spike trains from extracellular recordings of behaving ferrets. Section 7 summarizes information on implementation and computational demands.

1. Maximum likelihood estimation for integrate-and-fire neurons

Maximum likelihood estimation is a principled method for fitting statistical models to observations. Given observed data D and a model that depends on a vector of parameters $\boldsymbol{\theta}$, the estimated value $\hat{\boldsymbol{\theta}}$ of the parameter vector is determined by maximizing the likelihood that the observations are generated by the model,

$$\hat{\boldsymbol{\theta}} := \mathrm{argmax}_{\boldsymbol{\theta}}\, p(\mathrm{D}|\boldsymbol{\theta}). \tag{1}$$

This method features several attractive properties, among them: (i) the distribution of maximum likelihood estimates is asymptotically Gaussian with mean given by the true value of $\boldsymbol{\theta}$; (ii) the variances of the parameter estimates achieve a theoretical lower bound, the Cramer-Rao bound (given by the reciprocal of the Fisher information) as the sample size increases [36]. It should further be noted that maximizing the likelihood $p(\mathrm{D}|\boldsymbol{\theta})$ within plausible limits for the parameter values is equivalent to maximizing the posterior probability density for the parameters given the data, $p(\boldsymbol{\theta}|\mathrm{D})$, without prior knowledge about the parameters except for the limits (i.e., assuming a uniform prior distribution of $\boldsymbol{\theta}$).

Let us first focus on single neurons (for networks see Results section 4). The data we have are neuronal spike times, which we collect in the ordered set

$$\mathrm{D} := \{t_1, \ldots, t_K\}. \tag{2}$$

We consider neuron models of the integrate-and-fire (I&F) type, which describe the membrane voltage dynamics by a differential equation together with a reset condition that simplifies the complex, but rather stereotyped, dynamics of action potentials (spikes). Here we focus on the classical leaky I&F model [37] but

also consider a refined variant that includes a nonlinear description of the spike-generating sodium current at spike initiation and is known as exponential I&F model [38]. An extended I&F model that accounts for neuronal (spike rate) adaptation [9, 39, 40] is included in Results section 5. Each model neuron receives fluctuating inputs described by a Gaussian white noise process with (time-varying) mean $\mu(t)$ and standard deviation σ.

We would like to point out that not all model parameters need to be estimated. The membrane voltage can be scaled such that the remaining parameters of interest for estimation are those for the input together with the membrane time constant τ_m in case of the leaky I&F model, and additionally the reset voltage V_r in case of the exponential I&F model (for details see Methods section 1).

We are interested in the likelihood $p(\mathrm{D}|\boldsymbol{\theta})$ of observing the spike train D from the model with parameter vector $\boldsymbol{\theta}$. As spike emission in I&F models is a renewal process (except in presence of adaptation, see below) this likelihood can be factorized as

$$p(\mathrm{D}|\boldsymbol{\theta}) = \prod_{k=1}^{K-1} p(t_{k+1}|t_k, \mu[t_k, t_{k+1}], \boldsymbol{\theta}), \tag{3}$$

where $\mu[t_k, t_{k+1}] := \{\mu(t) \,|\, t \in [t_k, t_{k+1}]\}$ denotes the mean input time series across the time interval $[t_k, t_{k+1}]$. In words, each factor in Eq. (3) is the probability density value of a spike time conditioned on knowledge about the previous spike time, the parameters contained in $\boldsymbol{\theta}$ and the mean input time series across the inter-spike interval (ISI). We assume that $\mu[t_k, t_{k+1}]$ can be determined using available knowledge, which includes the parameters in $\boldsymbol{\theta}$ as well as previous (observed) spike times.

For robust and rapid parameter estimation using established optimization techniques we need to compute $p(\mathrm{D}|\boldsymbol{\theta})$ as accurately *and* efficiently as possible. Typical simulation-based techniques are not well suited because they can only achieve a noisy approximation of the likelihood that depends on the realization of the input fluctuations and is difficult to maximize. This poses a methodological challenge which can be overcome using analytical tools that have been developed for I&F neurons in the context of the *forward* problem of calculating model output for given parameters [41–45]. These tools led us to the following methods that we explored for the *inverse* problem of parameter estimation:

- Method **1** calculates the factors of the likelihood (Eq. (3), right hand side) via the inter-spike interval (ISI) probability density p_ISI, using

  $$p(t_{k+1}|t_k, \mu[t_k, t_{k+1}], \boldsymbol{\theta}) = p_\mathrm{ISI}(s_k|\mu_\mathrm{ISI}[0, s_k], \boldsymbol{\theta}), \tag{4}$$

  where $s_k := t_{k+1} - t_k$ is the length of the k-th ISI and μ_ISI is the mean input across that ISI given by $\mu_\mathrm{ISI}[0, s_k] = \mu[t_k, t_{k+1}]$. We obtain p_ISI by solving a Fokker-Planck partial differential equation using two different numerical solution schemes which serve for different model scenarios (for details see Methods section 2). One of these schemes relies on the Fourier transform and provides an efficient approximation for small amplitude variations of the mean input,

  $$\mu(t) = \mu_0 + J\mu_1(t) \tag{5}$$

  $$p_\mathrm{ISI}(s_k|\mu_\mathrm{ISI}[0, s_k], \boldsymbol{\theta}) \approx p^0_\mathrm{ISI}(s_k|\mu^0_\mathrm{ISI}, \boldsymbol{\theta}) + J\, p^1_\mathrm{ISI}(s_k|\mu^1_\mathrm{ISI}[0, s_k], \boldsymbol{\theta}) \tag{6}$$

  with $\mu^0_\mathrm{ISI} = \mu_0$ and $\mu^1_\mathrm{ISI}[0, s_k] = \mu_1[t_k, t_{k+1}]$, for small $|J|$. We refer to it as method **1a**. The other numerical scheme employs a finite volume discretization and is accurate for arbitrary variations of the mean input but computationally more demanding. We refer to it as method **1b**.

- Method **2** uses an approximation of the spike train by an inhomogeneous Poisson (point) process. The spike rate $r(t)$ of that process is effectively described by a simple differential equation derived from the integrate-and-fire model and depends on the mean input up to time t as well as the other parameters in $\boldsymbol{\theta}$ (for details see Methods section 3). In this case the factors in Eq. (3), right, are expressed as

  $$p(t_{k+1}|t_k, \mu[t_k, t_{k+1}], \boldsymbol{\theta}) \approx r(t_{k+1}|\mu[t_1, t_{k+1}], \boldsymbol{\theta}) \exp\left(-\int_{t_k}^{t_{k+1}} r(\tau|\mu[t_1, \tau], \boldsymbol{\theta})\, d\tau\right). \tag{7}$$

The most accurate and advantageous method depends on the specific setting, as illustrated for different scenarios in the following sections.

2. Inference of background inputs

We first consider the spontaneous activity of an isolated recorded neuron. This situation is modeled with an I&F neuron receiving a stationary noisy background input with constant mean μ and standard deviation σ which are the parameters to be estimated. For this scenario method **1a** is very efficient and sufficiently accurate, and therefore well suited.

2.1 Evaluation using in-silico ground truth data

An example of the simulated ground truth data, which consists of the membrane voltage time series including spike times, is shown in Fig. 1A together with ISI and membrane voltage histograms. Note that for estimation we only use the spike times. By maximizing the likelihood (specifically, its logarithm, see Methods section 4) the true parameter values are well recovered (Fig. 1B) and we obtain an accurate estimate of the ISI density. In addition, we also obtain an accurate estimate for the (unobserved) membrane voltage density, which can be calculated using a slight modification of method **1** in a straightforward way once the parameter values are determined. Here the remaining parameter of interest, the membrane time constant τ_{m}, was set to the true value; fixing τ_{m} at a wrong value instead (e.g., with a relative error of 50 %) still leads to a good fit in terms of spike train likelihood (relative error < 0.1 %).

We next evaluated the estimation accuracy for different numbers of observed spikes (Fig. 1C). As little as 50 spikes already lead to a good solution with a maximum average relative error (with respect to the true parameter values) of about 10 %. Naturally, the estimation accuracy increases with the number of observed spikes. Moreover, the variance of the parameter estimates decreases as the number of spikes increases, and approaches the Cramer-Rao bound (which we calculated analytically, see Methods section 5) as expected for a maximum likelihood estimator. This quantity limits the variance of any unbiased estimator from below.

To further quantify how well the different parameters can be estimated from a spike train of a given length, we computed the Fisher information (per ISI), shown in Fig. 1D. For a reasonable range of input parameter values, we consistently find that μ is easier to estimate than σ. τ_{m} is clearly more difficult to estimate than both other parameters. For comparison, we considered the exponential I&F model which involves additional parameters (Fig. 1E): according to the Fisher information for this model, estimation of μ is again easier than σ, and τ_{m} is the most difficult to estimate. For each parameter, the Fisher information appears to vary weakly with the value of the parameter.

2.2 Validation using in-vitro ground truth data

We validated our inference method using somatic whole-cell recordings of cortical pyramidal cells (PYRs) [34] and fast-spiking interneurons (INTs) exposed to injected fluctuating currents. A range of stimulus statistics, in terms of different values for the mean μ_I and standard deviation σ_I of these noise currents, was applied and each cell responded to multiple different stimuli (examples are shown in Fig. 2A; for details see Methods section 7.1). We estimated the input parameters (μ and σ) of an I&F neuron from the observed spike train for each stimulus by maximizing the spike train likelihood. Note that since we considered only spikes, and not the membrane potential, we did not estimate the input resistance and rest potential; therefore, the input parameters were defined up to arbitrary offset and scale factors.

Model fitting yielded an accurate reproduction of the ISI distributions (Fig. 2A). Importantly, the estimated input statistics well captured the true stimulus statistics (Fig. 2B,C). In particular, estimated and true mean input as well as estimated and true input standard deviations were strongly correlated for all cells (Fig. 2 B, C). The correlation coefficients between estimated and ground truth values for INTs are larger than those for PYRs, as reflected by the concave shape of the estimated μ values as a function of μ_I. This shape indicates a saturation mechanism that is not included in the I&F model. Indeed, it can in part be explained by the intrinsic adaptation property of PYRs (see Results section 5 below). Furthermore, correlation coefficients are slightly increased for longer stimuli (15 s compared to 5 s duration) due to improved estimation accuracy for longer spike trains.

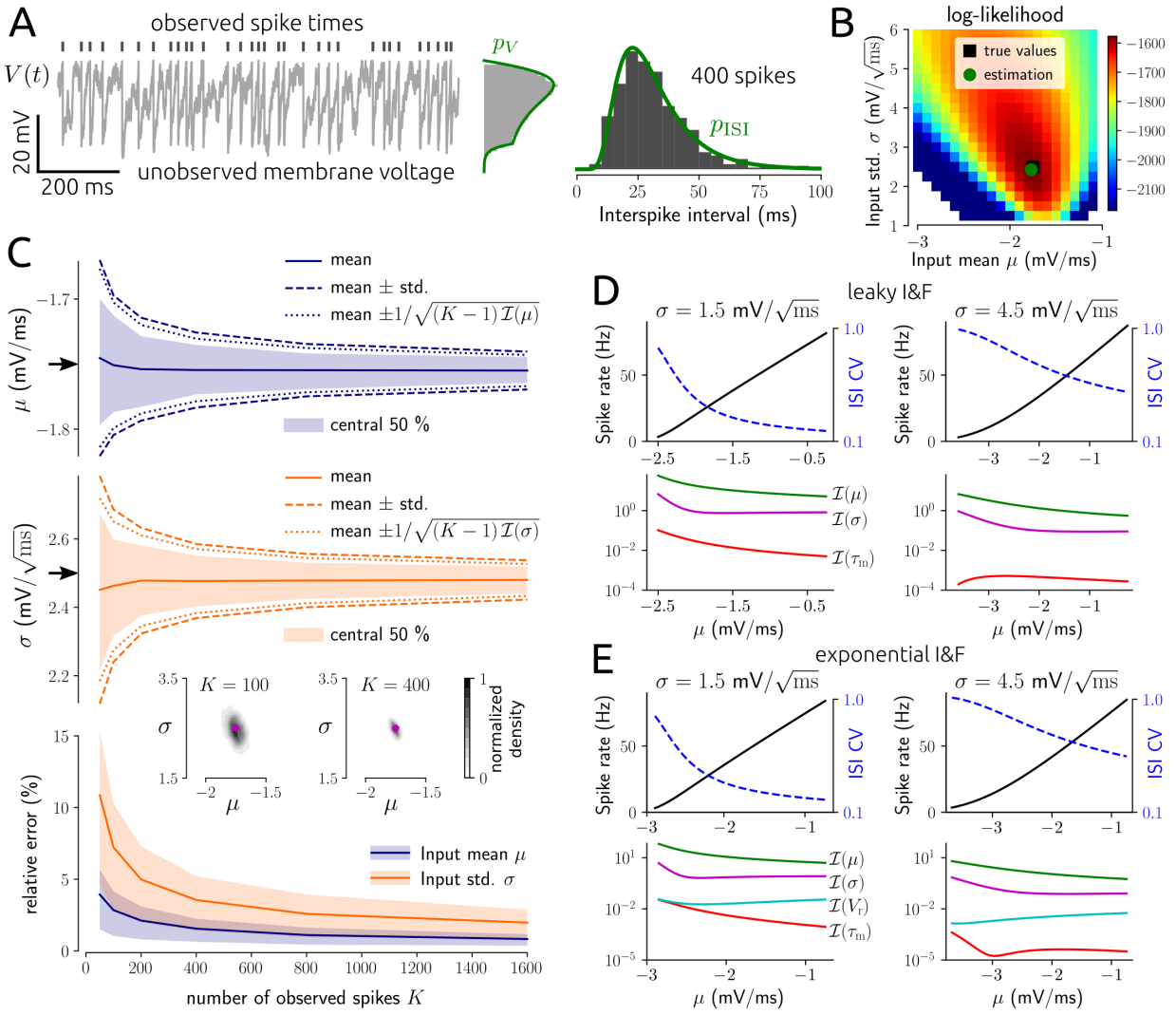

Figure 1. Estimation results for background input statistics using simulated data. **A**: example membrane voltage time series with indicated spike times from a leaky I&F neuron (Eqs. (9)–(11)) together with membrane voltage and ISI histograms, and associated densities p_V, p_{ISI} calculated using the Fokker-Planck equation (see Methods sections 2 and 3). Method **1a** was used for parameter estimation. **B**: log-likelihood $\log p(\mathrm{D}|\boldsymbol{\theta})$ as a function of the input mean μ and variance σ based on 400 spike times from the example in **A**, with true and estimated parameter values indicated. **C**: mean and central 50 % of estimates (i.e., 25$^{\mathrm{th}}$-75$^{\mathrm{th}}$ percentile) for μ and σ as a function of number of spikes K, together with standard deviation about the mean and the theoretical bound according to the Cramer-Rao inequality (see Methods section 5) indicated by dashed and dotted lines, respectively. Arrows mark true values. Bottom: mean and central 50 % of relative errors between estimated and true parameter values as a function of K. Insets: empirical density of estimated parameter values with true values indicated for $K = 100$ and $K = 400$. **D**: spike rate and ISI coefficient of variation (CV) calculated using the Fokker-Planck equation (see Methods sections 2 and 3) as a function of μ and σ, and Fisher Information per ISI ($\mathcal{I}$) for μ, σ and τ_{m}. **E**: same as **D** for the exponential I&F model instead of the leaky I&F model, including Fisher Information per ISI for the reset voltage V_{r}.

3. Inference of input perturbations

We next consider the effects of partially known, time-dependent inputs to the recorded neuron. These inputs may reflect hypothesized synaptic or stimulus-driven inputs at known times. Specifically, for the evaluation

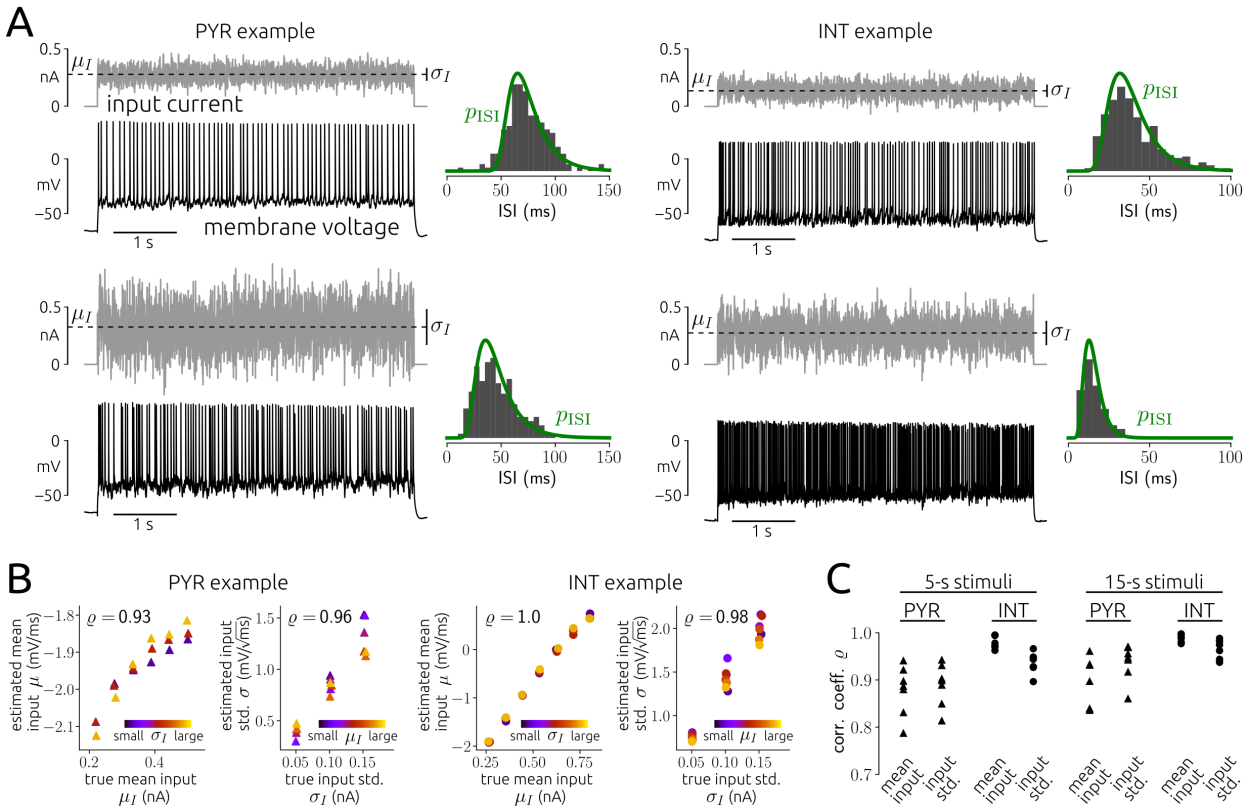

Figure 2. Estimation results for background input statistics using in-vitro data. A: examples of recorded membrane voltage in response to noise stimulus current with indicated mean μ_I and standard deviation σ_I (vertical bar marks $\mu_I \pm \sigma_I$) together with ISI histogram and density p_{ISI} that corresponds to the fitted I&F model for a PYR (left) and an INT (right). Method **1a** was used for parameter estimation. **B**: estimated input parameters (μ, σ) versus empirical input statistics (μ_I, σ_I) with Pearson correlation coefficient ϱ indicated for an example PYR and INT each. **C**: ϱ for input mean and standard deviation for all seven PYRs and six INTs and for two stimulus durations.

we consider $\mu(t) = \mu_0 + J\mu_1(t)$, where μ_0 denotes the background mean input (cf. Results section 2) and $\mu_1(t)$ is described by the superposition of alpha functions with time constant τ, which are triggered at known times (for details see Methods section 1). These times can be thought of, for example, as observed spike times of another (pre-synaptic) neuron. We estimate the perturbation strength J as well as τ which determines the temporal extent over which the perturbation acts. For this scenario we apply and compare the methods **1a** and **2**. Method **1b** is computationally too costly here because p_{ISI} needs to be computed for each ISI separately (since the mean input variation across an ISI depends on the time of ISI onset relative to the trigger times).

Estimation accuracy for a range of perturbation strengths is shown in Fig. 3A,B. Note that the input perturbations are relatively weak, producing mild deflections of the membrane voltage which are difficult to recognize visually in the membrane voltage time series in the presence of noisy background input (Fig. 3A). Both methods perform comparably well for weak input perturbations. As $|J|$ increases the estimation accuracy of method **2** increases, whereas that of method **1a** decreases (Fig. 3B) because it is based on a linear, weak coupling approximation.

We further assessed the sensitivity of the estimation methods to detect (weak) input perturbations in comparison to a model-free method based on cross-correlograms (CCGs) between spike trains and perturbation times (Fig. 3C,D; for details see Methods section 6). The model-free approach estimates the probability that the input and the spike train are coupled, but does not provide additional information on the shape of that

coupling. Both model-based estimation methods are more sensitive in detecting weak perturbations than the model-free approach, with method **1a** expectedly performing best (Fig. 3D).

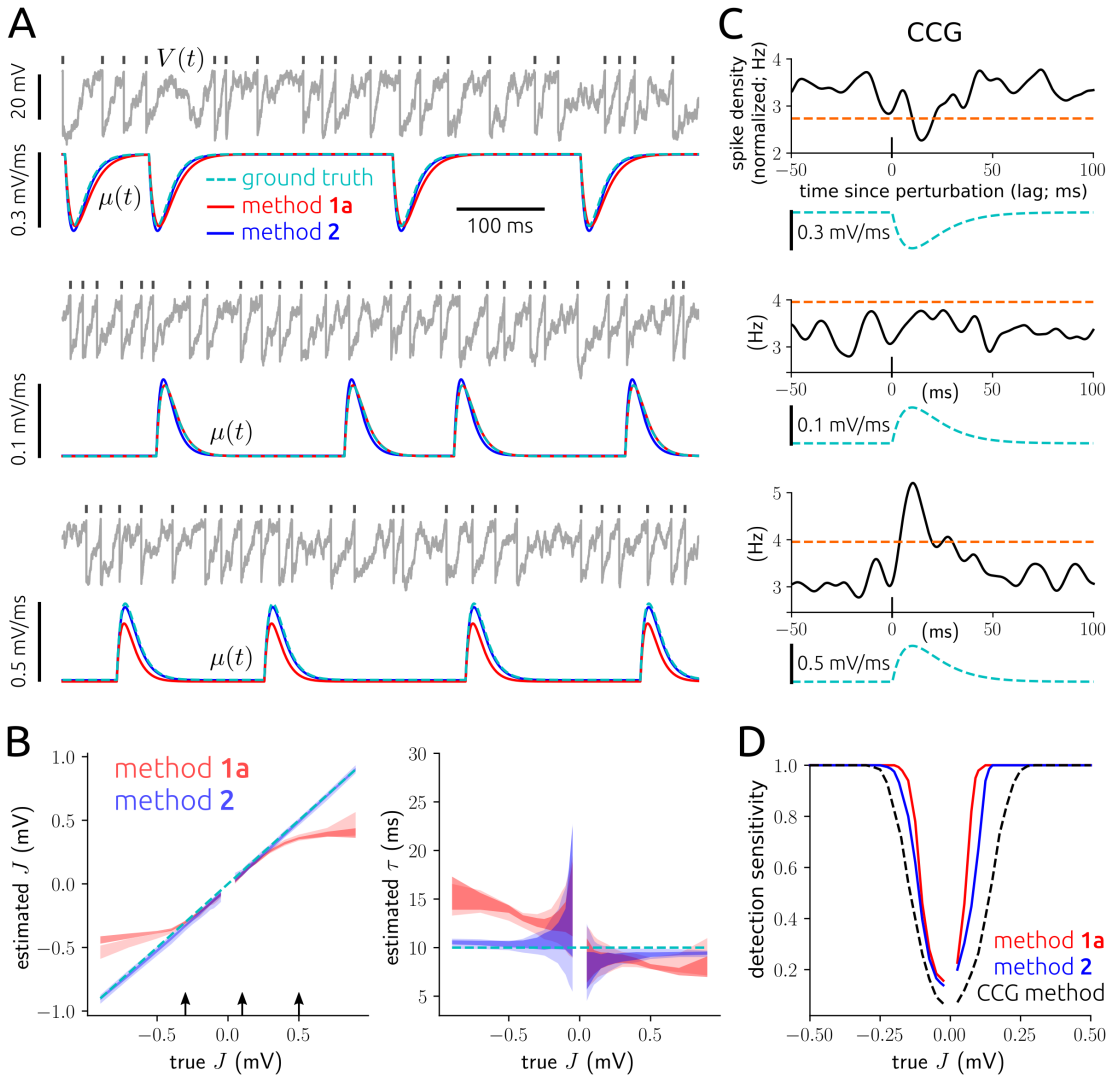

Figure 3. Estimation results for input perturbations. **A**: three example membrane voltage and mean input time series (true and reconstructed ones using the estimated parameter values) for weak excitatory (center) and somewhat stronger inhibitory (top) and excitatory (bottom) perturbations. Methods **1a** and **2** were used for parameter estimation. **B**: central 50 % of estimates (i.e., 25^{th}-75^{th} percentile) for J and τ as a function of true J for two spike train lengths (100 s, light color; 500 s, dark color). Arrows indicate the parameter choices in **A**. **C**: normalized CCGs (i.e., spike density curves aligned to perturbation onset times), with significance threshold (orange dashed) for the indicated mean input perturbations, corresponding to the examples in **A**. The CCGs are normalized such that their integral over all lags equals 1. **D**: detection sensitivity as a function of J computed from the estimation methods (solid lines) or using CCGs (dashed line) based on spike trains of length 100 s (cf. **C**). For details see Methods section 6.

4. Inference of synaptic coupling

In the previous section we showed that we can successfully estimate the perturbations in the spiking of an individual neuron that may be elicited by inputs from another neuron. We now turn to estimating synaptic

couplings in a network. We consider the situation in which we have observed spike trains of N neurons. We fit these data using a network model in which each neuron i receives independent fluctuating background input with (neuron-specific) mean and variance μ_i and σ_i^2, and neurons are coupled through delayed current pulses which cause post-synaptic potentials of size $J_{i,j}$, for $i, j \in \{1, \ldots, N\}$. Our aim is therefore to estimate the coupling strengths in addition to the statistics of background inputs caused by unobserved neurons.

We collect the observed spike times of all N neurons in the set D and separate the matrix of coupling strengths $\mathbf{J}$ from all other parameters in $\boldsymbol{\theta}$ for improved clarity. Note that the overall mean input for neuron i can therefore be expressed as $\mu_i + \sum_{j=1}^{N} J_{i,j}\mu_j^1(t)$ where $J_{i,j}\mu_j^1(t)$ describes the synaptic input for neuron i elicited by neuron j. The likelihood $p(\mathrm{D}|\boldsymbol{\theta}, \mathbf{J})$ can be factorized into ISI probability density values, where each factor is determined by the parameters in $\boldsymbol{\theta}$ together with a specific subset of all coupling strengths and knowledge of the spike times that we have observed. Assuming reasonably weak coupling strengths each of these factors can be approximated by the sum of the ISI probability density value in absence of input perturbations and a first order correction due to neuronal coupling (cf. Eq. (6) and Methods section 2) to obtain

$$p(\mathrm{D}|\boldsymbol{\theta}, \mathbf{J}) \approx \prod_{i=1}^{N} \prod_{k=1}^{K_i - 1} p_{\mathrm{ISI}}^0(s_i^k|\mu_{\mathrm{ISI}}^0, \boldsymbol{\theta}) + \sum_{j=1}^{N} J_{i,j}\, p_{\mathrm{ISI}}^1(s_i^k|\mu_{\mathrm{ISI},j}^1[0, s_i^k], \boldsymbol{\theta}) \tag{8}$$

with $\mu_{\mathrm{ISI}}^0 = \mu_i$ and $\mu_{\mathrm{ISI},j}^1[0, s_i^k] = \mu_j^1[t_i^k, t_i^{k+1}]$, where t_i^k denotes the k-th of K_i observed spike times and $s_i^k := t_i^{k+1} - t_i^k$ the length of the k-th ISI of neuron i. Note that the mean input perturbations $\mu_{\mathrm{ISI},j}^1$ depend on the spike times of neuron j. The approximation (8) allows for the application of method **1a**, by which the likelihood can be calculated in an efficient way.

4.1 Evaluation using network simulations

We first evaluated our method on simulated ground truth data for relatively small ($N = 10$) as well as larger ($N = 50$) fully observed networks of neurons. The estimated parameters show a remarkable degree of accuracy (Fig. 4A-D).

In a realistic scenario, the N recorded neurons belong to a larger network that is sub-sampled through the measurement process. The unobserved neurons therefore contribute additional, hidden inputs. In the fitted model, the effect of these unobserved neurons on neuron i is absorbed in the estimated statistics (μ_i, σ_i) of the background noise. Specifically, the total external input of neuron i, originating from a large number M_i of unobserved neurons whose spike trains are represented by independent Poisson processes with rates r_j, can be approximated for reasonably small coupling strengths with a background noise of mean $\mu_i = \sum_{j=N+1}^{N+M_i} J_{i,j} r_j$ and variance $\sigma_i^2 = \sum_{j=N+1}^{N+M_i} J_{i,j}^2 r_j$ (diffusion approximation [46]). Because of shared connections from unobserved neurons, the inputs received by the different observed neurons are in general correlated, with correlation strength that depends on the degree of overlap between the unobserved pre-synaptic populations. The model we fit to the observed data however assumes uncorrelated background inputs (conditioned on possibly correlated means and variances).

To assess the influence of correlations due to unobserved common inputs, we first fitted our model to data generated from a network with correlated background inputs. The estimation accuracy of synaptic strengths is still good in case of weak correlations of the external input fluctuations (correlation coefficient $c \leq 0.05$ for each pair of observed neurons) but clearly decreases as these correlations increase (Fig. 4E). In particular, positive correlations $c > 0$ lead to an overestimation of the coupling strengths. Empirical values for these so-called noise correlations from experimental studies are typically very small [24, 47, 48].

We next evaluated our method on data generated by explicitly sub-sampling (partially observed) networks of 800 excitatory and 200 inhibitory neurons that were rather sparsely and randomly connected with probabilities 0.1-0.2 (Figs. 4F,G). Estimation accuracy of connectivity structure and coupling strengths was surprisingly good for sufficiently long simulated recordings in this scenario.

In sum, our approach yields good estimation results for sub-sampled networks as long as the correlations between the hidden (external) input fluctuations on a fine timescale are not too large. Notably, the method can further be accommodated for shared (unknown) variations of input statistics, and thus, time-varying spike rates, caused by unobserved neurons or network interaction (see next section).

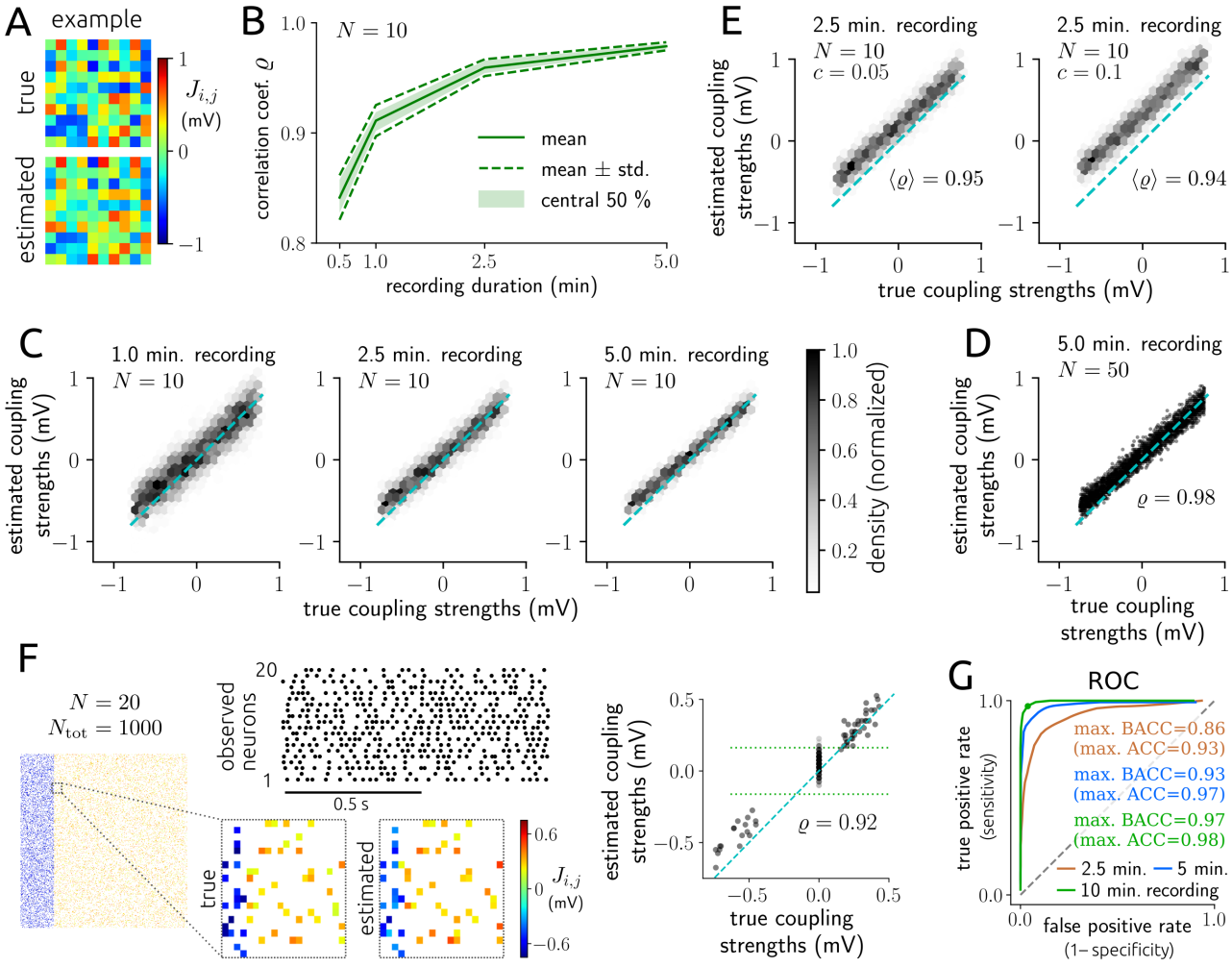

Figure 4. Estimation results for synaptic coupling strengths using simulated data. A: example coupling matrix (true and estimated) using a 5 min. long (simulated) recording of $N = 10$ spike trains and estimation method **1a**. **B**: Pearson correlation coefficient ϱ between true and estimated coupling strengths as a function of spike train length (simulated recording duration) from a large number of networks. **C**: density of estimated vs. true coupling strengths for 3 spike train lengths (corresponding to **B**). **D**: estimated vs. true coupling strengths from a network of $N = 50$ neurons. **E**: density of estimated vs. true coupling strengths for correlated external input fluctuations (input correlation coefficient $c = 0.05, 0.1$). In **A-D** we used $c = 0$. **F**: observed spike trains as well as true and estimated coupling strengths of $N = 20$ neurons from a randomly coupled network of $N_{\text{tot}} = 1000$ (800 excitatory, 200 inhibitory) neurons with connection probabilities 0.1 for excitatory and 0.2 for inhibitory synapses, heterogeneous (unknown) synaptic strengths and statistics of external inputs; $c = 0$. A discrimination threshold for the presence/absence of connections was applied (indicated by dotted lines; for details see Methods section 1). **G**: receiver operating characteristic (ROC) curves for the detection of synapses, i.e., true positive rate vs. false positive rate as the discrimination threshold varies. Solid lines represent averages over 3 networks. The green dot corresponds to the estimation result in **F**. Dashed line represents random guessing.

4.2 Validation using in-vivo ground truth data

We validated our inference of synaptic coupling using simultaneous extracellular recordings and juxtacellular stimulations of hippocampal neuronal ensembles in awake mice [35]. Following the approach developed in [35], we estimated connectivity by applying our model-based method to spontaneous, extracellularly

recorded spiking activity, and assessed the accuracy of our estimates by comparison with ground-truth data. Ground-truth connectivity was obtained by evoking spikes in single PYRs juxtacellularly using short current pulses, while recording extracellular spike trains of local INTs (for an example see Fig. 5A). Ground truth values for the presence and absence of synaptic connections were derived from spike train CCGs using the evoked presynaptic spikes, taking into account co-modulation caused by common network drive (for details see Methods section 7.2).

An important issue with respect to the basic assumptions of our model is that spontaneous activity appeared to be highly non-stationary, so that the spike trains of the recorded neurons were typically co-modulated. To infer synaptic couplings from the spontaneous spike trains with our model-based approach, we accounted for network co-modulation in two ways: (i) through small temporal perturbations of the PYR spike times, used to compute coupling strength z-scores; (ii) through estimated variations of the background mean input for the (potentially postsynaptic) INTs, that is, $\mu^0_{\mathrm{ISI}} = \mu_i$ in Eq. (8) was allowed to vary between ISIs. These variations were inferred from the instantaneous spike rate, which typically varied at multiple timescales over the duration of the recordings that lasted up to ∼2 h (Fig. 5A). We, therefore, estimated the variations of mean input at three different timescales separately and inferred synaptic couplings for each of these (see Methods section 7.2). In addition, we combined those results, using the largest absolute z-score across the three timescales for each connection.

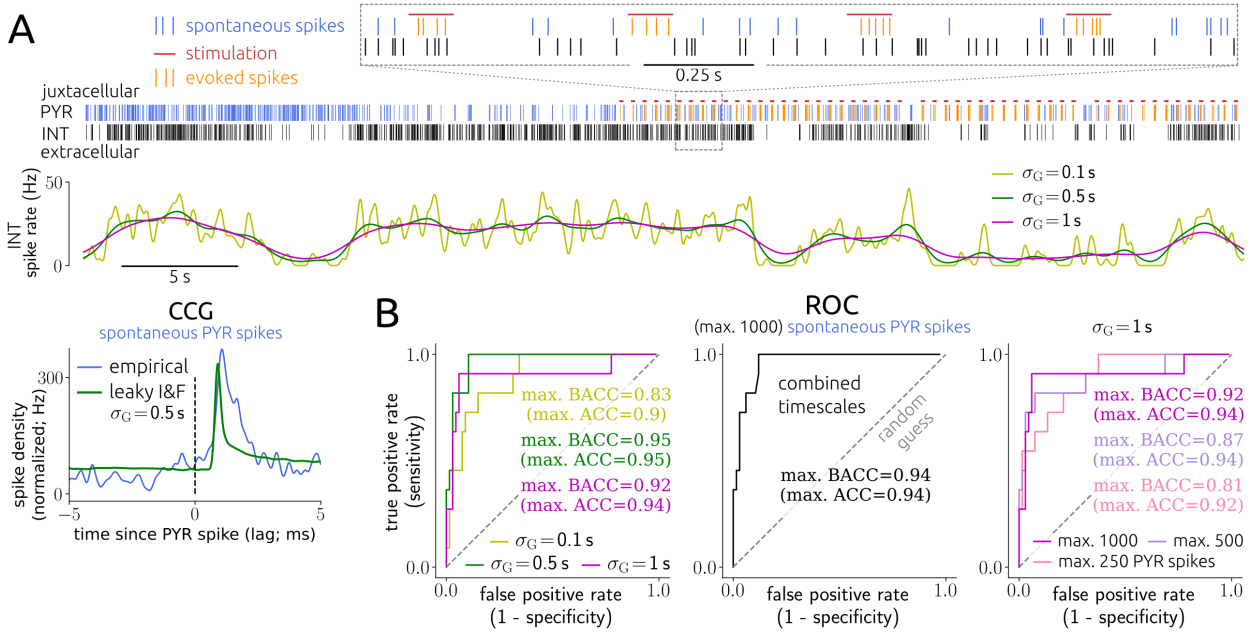

Figure 5. Estimation results for synaptic couplings using in-vivo data. **A**: example spike trains of a juxtacellularly recorded PYR and an extracellularly recorded INT, with stimulation pulses indicated (top panel). Instantaneous spike rate of the INT computed via kernel density estimation using a Gaussian kernel with width σ_{G} as indicated (center panel). Bottom: CCG between spontaneous PYR and INT spike times and as computed from an I&F neuron fitted to the INT spike train together with estimated coupling strength and delay. Method **1a** was used for parameter estimation. Note that CCGs were not used for model-based inference. **B**: ROC curves for 78 PYR-INT pairs using the spontaneous PYR spikes for three different values of σ_{G} (left), for the combined timescales inference variant (center), and for reduced numbers of PYR spikes (right).

Although spontaneous activity was highly non-stationary, our inference of the connectivity appeared to be very accurate. Comparisons with ground truth estimates demonstrated (balanced) accuracy of up to 0.95 (for the intermediate timescale variant; Fig. 5B). Moreover, reducing the number of spikes used for inference did not lead to an appreciable decrease of reproduction accuracy. Notably, our method exhibited high sensitivity as revealed by large z-score values for all true connections (2.47-7.36) and maximal accuracy attained at a

large discrimination value ($J^z_{\text{thresh}} = 3.49$) for the combined timescales variant; when using all instead of max. 1000 PYR spikes for estimation that discrimination value becomes even larger ($J^z_{\text{thresh}} = 8.09$).

5. Inference of neuronal adaptation

We next extend the model neurons to account for spike rate adaptation – an important property of many types of neurons, including pyramidal cells [49–51]. It can be observed by a gradual change in spiking activity following an immediate response upon an abrupt change of input strength, as shown in Fig. 6A (see also Fig. 7A). This behavior is typically mediated by a slowly decaying transmembrane potassium current, which rapidly accumulates when the neuron spikes repeatedly. In the extended I&F neuron model [39, 40] this adaptation current is represented by an additional variable w that is incremented at spike times by a value Δw, exponentially decays with (slow) time constant τ_w in between spikes, and subtracts from the mean input μ_0, acting as a negative feedback to the membrane voltage (Fig. 6A, see Methods section 1).

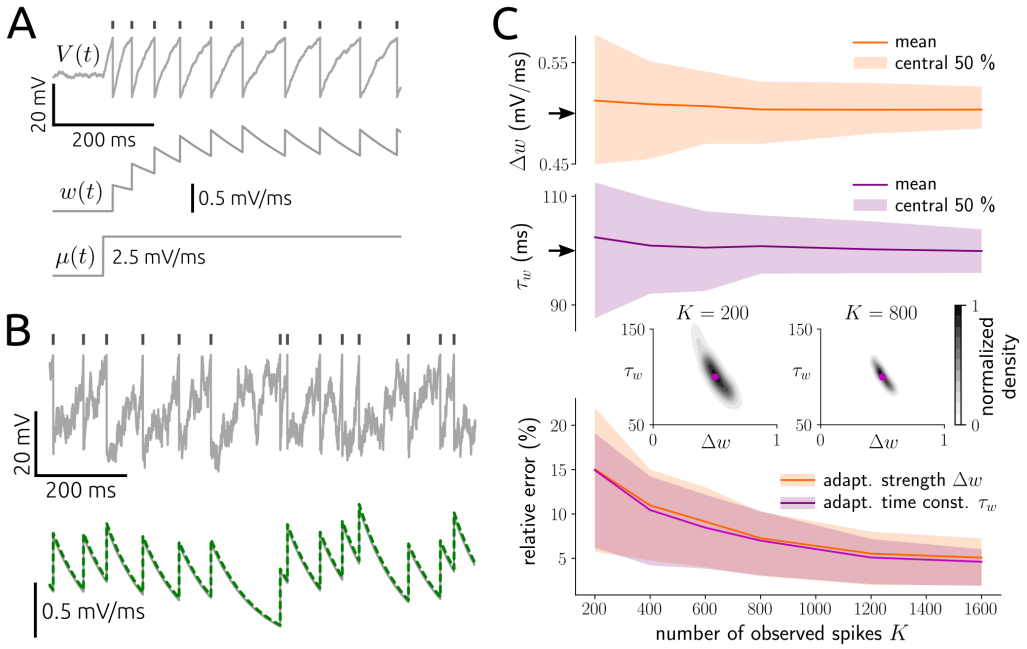

Figure 6. Estimation results for neuronal adaptation using simulated data. **A**: membrane voltage with indicated spike times (top) and adaptation variable (center) of an adaptive leaky I&F neuron in response to a step of mean input (bottom, for small input noise intensity σ). **B**: example membrane voltage and true adaptation current time series as well as the reconstruction using estimated adaptation parameters Δw, τ_w (based on 1000 spikes) and the observed spike times. The adaptation current is considered as normalized by the (unknown) membrane capacitance and therefore in units of mV/ms. Method **1b** was used for estimation. **C**: mean and central 50 % of estimates (i.e., 25^{th}-75^{th} percentile) for Δw and τ_w as a function of number of spikes K. Bottom: mean and central 50 % of relative errors between estimated and true parameter values as a function of K. Insets: empirical density of estimated parameter values with true values indicated for $K = 200$ and $K = 800$.

In contrast to classical I&F neurons, in the generalized model with adaptation, spiking is not a renewal process: given a spike time t_k the probability of the next spike depends on all previous spike times. That dependence is however indirect, as it is mediated through the effective mean input $\mu(t) - w(t)$ across the ISI $[t_k, t_{k+1}]$. This effective mean input can be explicitly expressed using the parameter values in $\boldsymbol{\theta}$ together with the observed spike times, and then inserted in Eqs. (3) and (4) for estimation. Here, method **1b** is best suited and can be applied efficiently by exploiting the fact that w varies within ISIs in a rather stereotyped way; that is, p_{ISI} does not need to be computed for each ISI separately (for details see Methods section 1).

Methods **1a** and **2** are less well suited for this scenario because the adaptation variable can accumulate to substantial values, thereby opposing the assumption of weak variations of the mean input; moreover, the spike train of an adapting neuron deviates strongly from a Poisson process.

5.1 Evaluation using in-silico ground truth data

We first evaluated the inference method using simulated ground truth for constant statistics of the background inputs (cf. Results section 1). An example of the membrane voltage and adaptation current time series is depicted in Fig. 6B. The true values for the adaptation parameters (the strength Δw and time constant τ_w) are well recovered and we obtain an accurate estimate of the adaptation current as it evolves over time. Here, too, the estimation accuracy depends on the number of observed spikes (Fig. 6C) and relative errors are on average less than 10 % for 500 spikes.

5.2 Validation using in-vitro recordings

To validate our inference method for adaptation parameters, we used the recordings of neurons stimulated by noise currents that we examined in Results section 2. Several cells, predominantly PYRs, exhibited spike rate adaptation (for an example see Fig. 7A). Accordingly, the adaptive I&F model yielded a clearly improved fit compared to the nonadaptive model for all but one PYRs as shown by the Akaike information criterion (AIC), which takes into account both goodness of fit and complexity of a model (Fig. 7B; for details see Methods section 7.1). On the other hand, for all except one INTs the nonadaptive model turned out to be the preferred one, which is consistent with the observation that INTs (generally) exhibit little spike rate adaptation compared to PYRs [52].

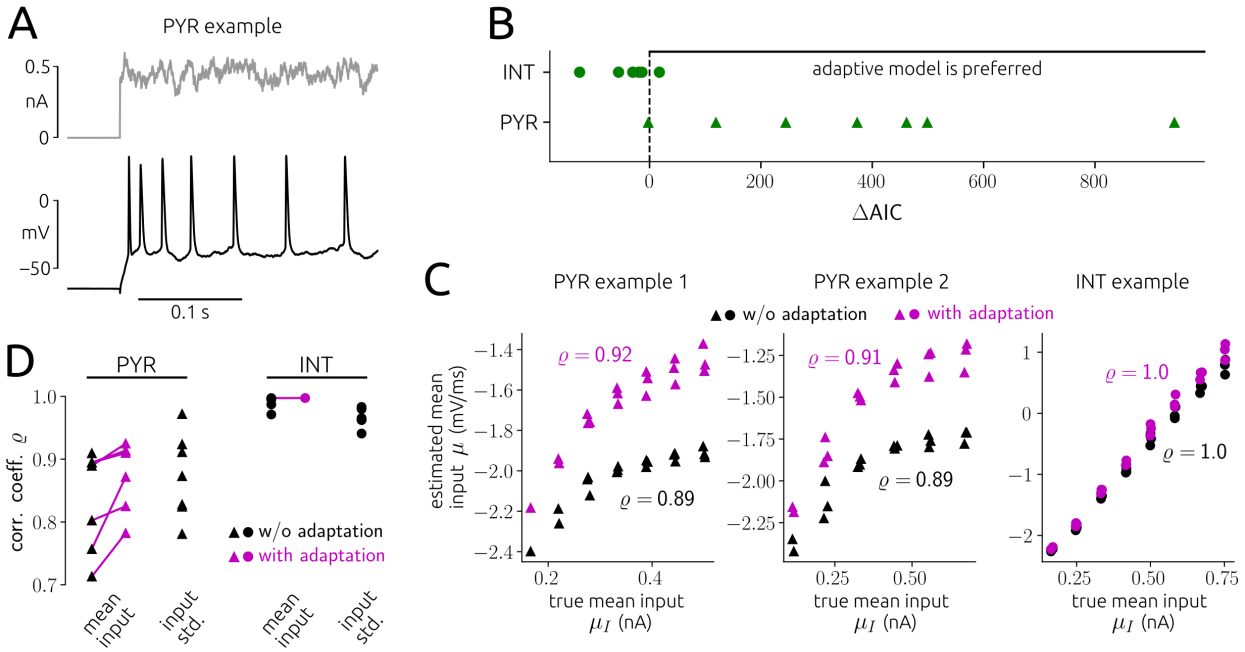

Figure 7. Comparison between inferred adaptive and nonadaptive models using in-vitro data. **A**: example recorded membrane voltage in response to an injected noisy step current showing spike rate adaptation. **B**: AIC difference (ΔAIC) between the nonadaptive and adaptive leaky I&F models for all seven PYRs and six INTs. **C**: estimated mean input μ as a function of empirical mean input μ_I for the adaptive and nonadaptive models (magenta and black symbols, respectively) for three example cells. ϱ denotes Pearson correlation coefficient. **D**: ϱ for input mean and standard deviation for the two models and all neurons. Estimation results in **B**-**D** were obtained using 15 s long stimuli.

We examined the mean input estimates from the adaptive model in comparison to the nonadaptive model for the neurons where the adaptive model was preferred (Fig. 7C,D). Note that the intrinsic adaptation current effectively subtracts from the mean input (but does not affect the input standard deviation). For all of those cells, including adaptation increased the correlation coefficient between estimated and empirical mean input. The remaining room for improvement of this correlation for PYRs indicates that there are likely multiple adaptation mechanisms (with different timescales) at work [52].

These results provide an indirect validation of our method and demonstrate its potential to infer intrinsic neuronal adaptation properties based on observed spike trains alone.

6. Estimation of neuronal inputs from in-vivo spike train data

Finally, we apply our method to spike train data obtained from extracellular multi-channel recordings in primary auditory cortex of awake behaving ferrets [53]. The animals were listening to regular sequences of click stimuli separated by periods of silence. Using a spike sorting algorithm, single unit spike trains were extracted (for details see Methods section 7.3).

We fitted a simple microcircuit model to these data. In the model, a leaky I&F model neuron received feed-forward excitatory and inhibitory inputs triggered by the clicks [17, 54, 55], as well as a fluctuating background input. The background input is characterized by its mean μ_0 and standard deviation σ, the click-triggered inputs are described using alpha functions with strengths J_e, J_i and time constants τ_e, τ_i, respectively. Note that this model is a slightly extended version of the one used in Results section 3. For each cell (single unit) we first estimated the parameters for the background input (with click-triggered inputs set to zero) from the spontaneous spike trains during periods of silence using method **1a**, and then estimated the parameters of the additional inputs from the data during click trains using method **2**.

To assess whether the complexity of this model is adequate given the available data we considered simpler models for comparison. For spontaneous activity, we compared our model to a Poisson process with constant rate. For click-evoked activity, we examined two additional models: (i) the leaky I&F model with only one (either excitatory or inhibitory) click-triggered input described by a delayed alpha function; (ii) a model in which the stimulus induced only a constant additional input. As a measure of quality we applied the AIC (cf. Results section 5).

The I&F model appears to be the preferred one for spontaneous activity for almost all cells according to the AIC (Fig. 8A). Examples of baseline data in terms of ISI histograms together with estimation results are shown in Fig. 8B, and estimated parameter values of the background input for all cells are visualized in Fig. 8C. The I&F model with fluctuating background input captures well a range of ISI histograms that characterize the baseline spiking activity of cortical neurons.

For click-evoked activity, the I&F model with click-triggered feed-forward excitatory and inhibitory inputs is the preferred one for 46 % of the cells, the simpler I&F model with a single click-triggered (dynamic) input is preferred for 14 % of the cells, and the I&F model with constant mean input fits best for 40 % of the cells which did not respond phasically to clicks. Examples of spiking activity across click trains measured by peri-stimulus time histograms (PSTHs) together with the spike rates and estimated click-triggered inputs of the fitted model neurons are shown in Fig. 8D, and distributions of the parameter estimates for the click-triggered inputs are visualized in Fig. 8E,F. It should be noted that the (trial-averaged) PSTHs were not used for parameter estimation, but they allow to conveniently visualize the spiking activity of real and model neurons. The estimated inputs generate spike rates that match well with a range of observed PSTHs.

In cells for which click-triggered excitatory-inhibitory inputs provided the best fits, we found that the values of the estimated input strengths and timescales were strongly correlated between the excitatory and the inhibitory components for each cell (Fig. 8E,F). Visual inspection shows that such balance between excitatory and inhibitory inputs is required to produce strongly biphasic responses to individual clicks seen in the PSTHs. This result is reminiscent of the finding (obtained through intra-cellular voltage-clamp recordings) that excitatory and inhibitory inputs are equalized throughout the population at the level of individual cells in the primary visual cortex [56]. Fitting only spike-trains, our approach therefore uncovers fundamental constraints on synaptic inputs and the local microcircuit without access to the values of the intra-cellular membrane potential.

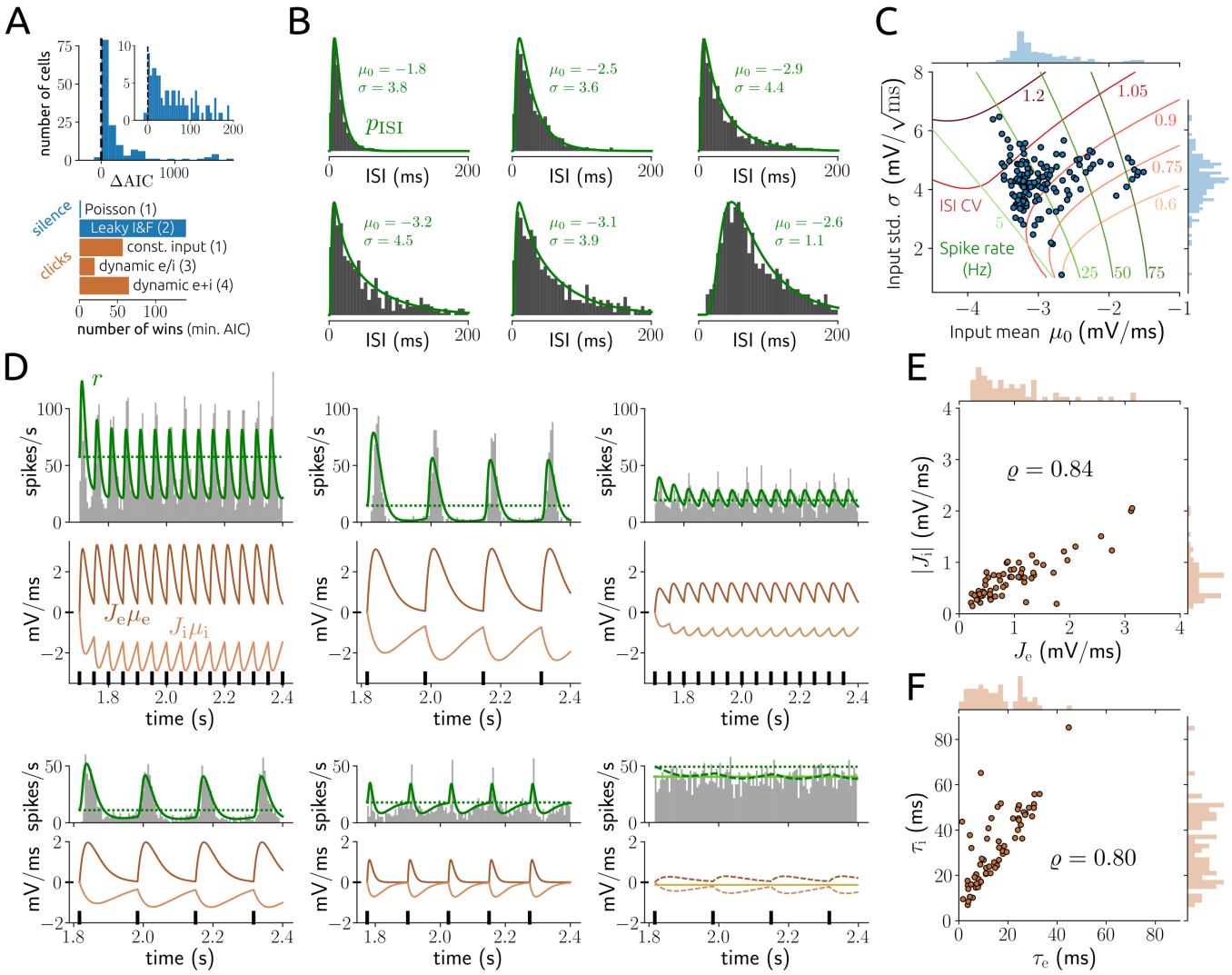

Figure 8. Estimation results using spike trains from in-vivo recordings in the ferret auditory cortex. **A**, top: histogram of AIC difference (ΔAIC) between the Poisson and I&F models for spontaneous activity (silence); bottom: number of wins according to AIC for the models compared for spontaneous and click-evoked activity (dynamic e/i: I&F with click-triggered excitatory or inhibitory input, dynamic e+i: I&F with click-triggered excitatory and inhibitory inputs). Numbers of estimated parameters are indicated in parentheses. For details see Methods section 7. **B**: examples of baseline ISI histograms and densities p_{ISI} (from method **1a**) that correspond to the estimated parameter values for the leaky I&F model (indicated). **C**: estimates of parameters for the background input together with lines of equal spike rate and ISI coefficient of variation (CV) calculated from p_{ISI}. **D**: examples of PSTHs across the click train periods and spike rates r (from method **2**) that correspond to the estimated parameter values for the dynamic e+i model; below, time series of the click-triggered inputs with click times indicated. Dotted lines visualize the estimated baseline spike rates. In the last example (bottom right) the model with constant input (solid lines) performed best. **E**, **F**: estimated magnitudes (J_e, $|J_i|$) and time constants (τ_e, τ_i) of the click-triggered inputs for cells where the dynamic e+i model was preferred according to AIC. Pearson correlation coefficients (ϱ) are indicated.

7. Implementation and computational complexity

We have implemented all three methods for parameter estimation using the Python programming language and applying the libraries Scipy [57] for optimization and Numba [58] for low-level machine acceleration. The

code for representative estimation examples from sections 2–5 is available as open source software under a free license at GitHub: https://github.com/neuromethods/inference-for-integrate-and-fire-models. Computation times for example inference problems are summarized in table 1.

Table 1. Computation times for estimation examples in Figs. 1–6.

Figure	1A	3A†		4A‡	4D‡	4G‡	6B
Method	**1a**	**1a**	**2**	**1a**	**1a**	**1a**	**1b**
Multiprocessing	no	no	no	yes	yes	yes	no
Estimation times (min.)	< 0.2	< 10	< 2	< 2.5	< 25	3.5–8.5	< 7

All computations were performed on a hexa-core personal computer. †Applies to each of the three examples. ‡Computation time scaled sub-linearly with recording time (hence with number of observed spikes) and supra-linearly with number of observed neurons.

Discussion

We presented efficient methods to fit simple integrate-and-fire circuit models to single-trial spike train data, and we evaluated and validated them extensively using in-silico, in-vitro and in-vivo ground truth data. Our approach allows to accurately infer hidden neuronal input statistics and adaptation currents as well as coupling strengths for I&F networks. We demonstrated that (i) the mean and variance of neuronal inputs are well recovered even for relatively short spike trains; (ii) for a sufficient, experimentally plausible number of spikes, weak input perturbations are detected with high sensitivity, (iii) coupling strengths are faithfully estimated even for partially observed (sub-sampled) networks, and (iv) neuronal adaptation strength and timescale are accurately inferred. By applying our methods to suitable electrophysiological datasets, we successfully validated our approach on inference of the statistics for in-vivo-like fluctuating inputs, intrinsic adaptation mechanisms, as well as in-vivo synaptic connectivity. Finally, we showed as a proof of principle that our methods can provide insights about local micro-circuitry using data from extracellular recordings of awake behaving animals.

Related approaches

Previously a small number of likelihood-based methods related to ours have been proposed, considering uncoupled I&F neurons with [59] or without adaptation [28,60,61] for constant [60] or time-varying [28,59,61] input statistics. The methods presented in Refs. [60, 61] only rely on observed spike trains, while those in Refs. [28, 59] additionally require the neuronal (mean) input time series to be known. All of these approaches employ the Fokker-Planck equation and numerically calculate the spike train likelihood [60] or use approximations [28,59,61]. Therefore, our methods differ from and extend the mentioned approaches in that they allow to efficiently infer, *without* knowledge of the neuronal input, (i) background input statistics for *nonlinear* I&F neurons, (ii) *synaptic coupling* of neuronal networks, and (iii) neuronal *adaptation* properties.

In the absence of likelihoods, methods for parameter fitting typically involve numerical simulations and distance measures that are defined on possibly multiple features of interest [31–33, 62, 63]. Evolutionary algorithms [31,32,62], brute-force search [33] or more principled Bayesian techniques [63] are then used to minimize the distances between observed and model-derived features. While these likelihood-free, simulation-based methods can be applied to more complex models they exhibit two disadvantages: the distance measures usually depend on (additional) parameters and their evaluation depends on the particular realization of noise or randomness considered in the model. Optimization can therefore be exceedingly time-consuming.

Estimation of synaptic coupling

Here we directly estimated synaptic coupling strengths for leaky I&F networks with fluctuating external inputs from observed spike trains. Our method is conceptually similar to those presented in [64, 65], but does not rely on an approximation of the ISI probability density that assumes vanishing [64] or small [65] amplitudes of input fluctuations (background noise).

We validated our approach first using simulations of network models. Applying our methods to a subset of randomly selected neurons, we found that our approach accurately uncovers the true connections and coupling strengths in spite of co-modulation from unobserved units in the network. We next tested our approach on in-vivo, extracellularly recorded data [35]. Comparison with ground-truth estimates obtained using juxta-cellular stimulations showed that our methods accurately identified the existing connections, although the network activity was highly non-stationary and generated strong co-modulations. Note that in that case, we did not have access to ground truth estimates of coupling strengths, and could therefore only validate the detection of connections.

Alternative approaches to infer connectivity from spike trains have employed phenomenological, generalized linear models [3,35,66], models of sparsely and linearly interacting point processes [67], or have been designed in a model-free manner, for example, using spike train cross-correlations [35, 68]. One of the advantages of our approach is that it includes an explicit (principled) mechanism to account for the effects of unobserved units (network co-modulation) which are condensed in the estimated dynamics of the background mean input for each neuron. This enables to better isolate pairwise interactions from (ubiquitous) fluctuating drive which has the potential to synchronize neurons that lack direct synaptic coupling. Considering its demonstrated high sensitivity to detect elicited weak inputs (cf. Fig. 3D), excellent agreement with (CCG-derived) ground truth (cf. Fig. 5) and superior fitting performance compared to simpler models in a basic setting (cf. Fig. 8A) our mechanistic model approach thus seems promising for inference of couplings in comparison with more phenomenological approaches.

Several related studies have focused on a theoretical link between network structure and correlated spiking activity recorded from a large number of neurons (without attempt to explicitly estimate synaptic connections) [69–73] and [74] for review. Of major relevance in this regard is the extent to which effective interactions among observed neurons are reshaped by coupling to unobserved neurons [75, 76]. Current methods to estimate coupling strengths from observed spike trains may be further advanced using these theoretical insights.

Possible methodological extensions

Here we described synaptic interaction by a simple form of delayed current pulses that cause (connection-specific) post-synaptic potentials. A conductance-based model of synaptic coupling could also be considered in principle. For this case the presented methods may be adjusted accordingly using results from [77], but it would generally complicate the calculations in methods **1** and **2**.

Throughout this work we assumed that the mean input trajectory across an ISI can be determined using available knowledge (e.g., about the parameters and previous spike times). A useful extension may be to incorporate an additional fluctuating component for the mean input, using a separate stochastic process that governs the evolution of $\mu(t)$ (on a slower time scale than the fluctuations $\xi(t)$), which results in a doubly stochastic model [61]. This could be advantageous for assessing shared variations of the external drive in terms of correlated fluctuating mean input caused from unobserved neurons on the population level. Here we accounted for network co-modulation by estimating the mean input dynamics from instantaneous neuronal spike rates at multiple (chosen) timescales (cf. Results section 4.2). A doubly stochastic model would allow to extract the most appropriate timescale from the data, which in turn could benefit the estimation of synaptic couplings using our mechanistic approach.

An important direction for future work would be to extend our approach to include various forms of synaptic plasticity, such as short-term depression/facilitation and spike-timing-dependent plasticity, and to infer its (additional) parameters from observed spike trains [78–80]. In term, short-term plasticity is particular apparent in in-vivo recordings [35], and including it in our models would be important for estimating coupling

strengths.

Towards a quantitative inference of neural circuits from spiking activity

Integrate-and-fire neurons are a popular tool for interpreting spiking activity in terms of simple circuit models (see, e.g., [13–15, 17–19]). Such approaches typically start by hypothesizing a structure for the underlying circuit based on available physiological information, and then examine the behavior of the resulting model as a function of the critical biophysical parameters. The model is then validated by qualitatively comparing the model output with experimental data. Specifically, the model activity is required to resemble key features of the experimental data in an extended region of the parameter space. If that is not the case, the model is rejected and a different one is sought.

An important benefit of this approach is that it provides a mechanistic interpretation and understanding of recorded activity in terms of biological parameters in a neural circuit. A major limitation is, however, that it typically relies on a qualitative comparison with the data to select or reject models. The methods presented here open the door to a more quantitative, data-driven approach, in which mechanistic circuit models can be evaluated and compared based on their fitting performance (cf. Figs. 7B and 8A for such comparisons) as is routinely the case for more abstract statistical models (see, e.g., [4]).

Materials and Methods

1. Neuron and network models

1.1 Integrate-and-fire neuron models

We consider typical I&F models subject to a fluctuating input. The dynamics of the membrane voltage V are governed by

$$\frac{dV}{dt} = f(V) + \mu(t) + \sigma\xi(t) \tag{9}$$

$$\text{if } V(t) \geq V_\text{s} \text{ then } V(t) \leftarrow V_\text{r}, \tag{10}$$

where μ is the mean input, σ the standard deviation of the input, ξ a (unit) Gaussian white noise process, i.e., $\langle \xi(t)\xi(t+\tau)\rangle = \delta(\tau)$ with expectation $\langle\cdot\rangle$, V_s is the threshold (or spike) voltage and V_r the reset voltage. For the leaky I&F model the function f is given by

$$f(V) := -\frac{V}{\tau_\text{m}} \tag{11}$$

where τ_m denotes the membrane time constant, whereas for the exponential I&F model f is defined by

$$f(V) := \frac{\Delta_\text{T}}{\tau_\text{m}} \exp\left(\frac{V - V_\text{T}}{\Delta_\text{T}}\right) - \frac{V}{\tau_\text{m}}, \tag{12}$$

where Δ_T is the threshold slope factor and V_T denotes the effective threshold voltage. The exponential term in Eq. (12) effectively approximates the rapidly increasing Na^+ current at spike initiation [38] and yields an improved fit to intracellular measurements of current-voltage relationships (typically obtained in-vitro) [7, 11]. For the exponential I&F model V_s does not play an important role as long as it is sufficiently larger than the effective threshold V_T. In fact, when V increases beyond V_T, it diverges to infinity in finite time due to the exponential term, which defines a spike. In practice, however, the spike is said to occur when V reaches V_s. It should be noted that for the methods used in this paper f can be any arbitrary (well-behaved) real-valued function.

The parameter values were $V_\text{s} = -40$ mV, $V_\text{r} = -70$ mV, $\tau_\text{m} = 20$ ms, $\Delta_\text{T} = 1.5$ mV, $V_\text{T} = -50$ mV, $\mu = -1.75$ mV/ms, $\sigma = 2.5$ mV/$\sqrt{\text{ms}}$ if not stated otherwise in figures or captions.

1.2 Voltage scaling

It is not meaningful to estimate all model parameters: a change of V_s or V_r in the leaky I&F model can be completely compensated in terms of spiking dynamics (in particular, the ISI density p_ISI) by appropriate changes of μ and σ; similarly, a change of V_T or Δ_T in the exponential I&F model can be completely compensated by appropriate changes of μ, σ, V_r and V_s. This can be seen using the change of variables $\tilde{V} := (V - V_\mathrm{r})/(V_\mathrm{s} - V_\mathrm{r})$ for the leaky I&F model and $\tilde{V} := (V - V_\mathrm{T})/\Delta_\mathrm{T}$ for the exponential I&F model model. Consequently, we may restrict the estimation to μ, σ, τ_m (leaky I&F model), and additionally V_r (exponential I&F model) and set the remaining parameters to reasonable values.

1.3 Input perturbations

In Results section 3 we consider input perturbations of the form $\mu(t) = \mu_0 + J\mu_1(t)$ (cf. Eq. (5)) with $\mu_1(t)$ given by the superposition of alpha functions with time constant τ, triggered at times $\tilde{t}_1, \ldots, \tilde{t}_L$,

$$\mu_1(t) = \sum_{l=1}^{L} H(t - \tilde{t}_l) \frac{t - \tilde{t}_l}{\tau} \exp\left(1 - \frac{t - \tilde{t}_l}{\tau}\right) \tag{13}$$

with Heaviside step function H. The alpha functions are normalized such that their maximum value is 1 (when considered in isolation). The perturbation onset (trigger) times were generated by randomly sampling successive separation intervals $\tilde{t}_{l+1} - \tilde{t}_l$ from a Gaussian distribution with 200 ms mean and 50 ms standard deviation.

1.4 Network model

In Results section 4 we consider networks of N_tot coupled leaky I&F neurons from which the spike trains of $N \leq N_\mathrm{tot}$ neurons have been observed. These networks are given by

$$\frac{dV_i}{dt} = -\frac{V_i}{\tau_\mathrm{m}} + \mu_i(t) + \sum_{j=1}^{N_\mathrm{tot}} J_{i,j}\mu_j^1(t) + \sigma_i\eta_i(t) \tag{14}$$

$$\mu_i^1(t) = \sum_{k=1}^{K_i} \delta(t - t_i^k - d) \tag{15}$$

$$\text{if } V_i(t) \geq V_\mathrm{s} \text{ then } V_i(t) \leftarrow V_\mathrm{r} \tag{16}$$

for $i \in \{1, \ldots, N_\mathrm{tot}\}$, where $J_{i,j}$ denotes the coupling strength between pre-synaptic neuron j and post-synaptic neuron i, t_i^k is the k-th of K_i spike times of neuron i, and d is the delay which we set to 1 ms. η_i describes the fluctuations of external input received from unobserved neurons,

$$\eta_i(t) = \sqrt{1 - c}\,\xi_i(t) + \sqrt{c}\,\xi_c(t), \tag{17}$$

where ξ_i, ξ_c are independent unit Gaussian white noise processes, i.e., $\langle \xi_i(t)\xi_j(t + \tau)\rangle = \delta_{ij}\delta(\tau)$, $i, j \in \{1, \ldots, N_\mathrm{tot}, c\}$, and c is the input correlation coefficient. We exclude autapses, i.e., $J_{i,i} = 0$, and consider uncorrelated or weakly correlated external input fluctuations, $0 \leq c \leq 0.1$. Note that the input variation for neuron i caused by neuron j across the interval $[t_i^k, t_i^{k+1}]$, denoted by $J_{i,j}\mu_j^1[t_i^k, t_i^{k+1}]$ (as used in Eq. (8)), is determined by the (observed) spike times of neuron j that occur in the interval $[t_i^k - d, t_i^{k+1} - d]$. In Results section 4.1 the mean input $\mu_i(t)$ was assumed constant, whereas in section 4.2 it varied between ISIs.

The (logarithmized) spike train likelihood (8) was optimized in the following way, justified by the assumption of (reasonably) weak coupling: first, the parameters for the background input were estimated for each neuron in isolation (all $J_{i,j} = 0$); then, the coupling strength $J_{i,j}$ was estimated given $\mu_i(t)$ and σ_i for each i, j - pair.

Network simulations for Figs. 4F,G were performed using the Python-based Brian2 simulator [81]. A discrimination threshold J_thresh for the presence/absence of connections was applied to estimated coupling

strengths $\hat{J}_{i,j}$. Accordingly, the presence of a connection (i,j - pair) was assured by the condition $|\hat{J}_{i,j}| > J_{\text{thresh}}$. The true positive rate (sensitivity) was given by the number TP of connections for which the estimation satisfied $|\hat{J}_{i,j}| > J_{\text{thresh}}$ and a true connection was present ($|J_{i,j}| > 0$), divided by the number P of true connections. The true negative rate (specificity) was given by the number TN of connections for which $|\hat{J}_{i,j}| \leq J_{\text{thresh}}$ and a true connection was absent ($J_{i,j} = 0$), divided by the number N of absent connections. Receiver operating characteristic (ROC) curves were generated from sensitivity and specificity as a function of J_{thresh}. Accuracy (ACC) and balanced accuracy (BACC) are defined as ACC = (TP + TN)/(P + N), BACC = (TP/P + TN/N)/2. The value of J_{thresh} used in Fig. 4F corresponds to the maximal BACC.

1.5 Spike rate adaptation

In Results section 5 we consider an extended I&F neuron model that includes an additional adaptation (current) variable w that is incremented at spike times, slowly decays, and counteracts the input to the neuron [39,40]: Eqs. (9) and (10) where the mean input $\mu(t)$ is replaced by an effective mean input $\mu(t) - w(t)$, with

$$\frac{dw}{dt} = -\frac{w}{\tau_w} \tag{18}$$

$$\text{if } V(t) \geq V_{\text{s}} \text{ then } w(t) \leftarrow w(t) + \Delta w. \tag{19}$$

τ_w is the adaptation time constant and Δw denotes the spike-triggered increment.

For known spike times (contained in set D) the effective mean input can be written as $\mu(t) - \Delta w\, \mu_1(t|\text{D}, \tau_w)$, where μ_1 between spike times t_k and t_{k+1} is explicitly expressed by

$$\mu_1(t|\text{D}, \tau_w) = \sum_{i=1}^{k} H(t - t_i) \exp\left(-\frac{t - t_i}{\tau_w}\right), \tag{20}$$

$t \in [t_k, t_{k+1}]$, with Heaviside step function H, assuming the adaptation current just prior to the first spike is zero, $w(t_1^-) = 0$. This means, for given parameters μ, Δw, τ_w the effective mean input time series is determined by the observed spike train (up to t_k). Note, that in general the mean input perturbations caused by adaptation vary from spike to spike, $\mu_1(t_k|\text{D}, \tau_w) \neq \mu_1(t_l|\text{D}, \tau_w)$ for $t_k \neq t_l \in \text{D}$. To efficiently evaluate the likelihood $p(\text{D}|\boldsymbol{\theta})$ using Eqs. (3) and (4) we calculate $p_{\text{ISI}}(s|\mu_{\text{ISI}}[0, s], \boldsymbol{\theta})$ with $\mu_{\text{ISI}}(s) = \mu(s) - w_0 \exp(-s/\tau_w)$, $s \geq 0$ for a reasonable range of values for w_0 and interpolate to obtain $p_{\text{ISI}}(s_k|\mu_{\text{ISI}}[0, s_k], \boldsymbol{\theta})$ with $\mu_{\text{ISI}}[0, s_k] = \mu[t_k, t_{k+1}] - \Delta w\, \mu_1[t_k, t_{k+1}]$ using Eq. (20).

2. Method 1: calculation of ISI density

Given a spike at $t = t_0$ the probability density of the next spike time is equal to the ISI probability density $p_{\text{ISI}}(s)$ where $s := t - t_0 \geq 0$ denotes the time since the last spike. This quantity can be approximated by numerical simulation in an intuitive way: starting with initial condition $V(t_0) = V_{\text{r}}$ one follows the neuronal dynamics given by Eq. (9) in each of n realizations (of the noise process) until the membrane voltage crosses the value V_{s} and records that spike time t_i (i-th realization). The set of times $\{t_i\}$ can then be used to compute p_{ISI}, where the approximation error decreases as n increases. Fortunately, we can calculate p_{ISI} analytically in the limit $n \to \infty$ by solving the Fokker-Planck partial differential equation (PDE) [82,83] that governs the dynamics of the membrane voltage probability density $p_V(V, s)$,

$$\frac{\partial p_V}{\partial s} + \frac{\partial q_V}{\partial V} = 0 \tag{21}$$

$$q_V := [f(V) + \mu_{\text{ISI}}(s)]\, p_V - \frac{\sigma^2}{2} \frac{\partial p_V}{\partial V} \tag{22}$$

with mean input $\mu_{\mathrm{ISI}}(s) = \mu(t)$ ($\mu_{\mathrm{ISI}}(s) = \mu(t) - w(t)$ in case of the adaptive I&F model, cf. Methods section 1.5), subject to the initial and boundary conditions

$$p_V(V, 0) = \delta(V - V_{\mathrm{r}}) \tag{23}$$

$$p_V(V_{\mathrm{s}}, s) = 0 \tag{24}$$

$$\lim_{V \searrow -\infty} q_V(V, s) = 0. \tag{25}$$

The ISI probability density is then given by the probability flux at V_{s},

$$p_{\mathrm{ISI}}(s|\mu_{\mathrm{ISI}}[0, s], \boldsymbol{\theta}) = q_V(V_{\mathrm{s}}, s). \tag{26}$$

In the field of probability theory p_{ISI} is also known as first passage time density.

2.1 Method 1a: numerical solution based on Fourier transform

The method described below is inspired by [41] and provides a solution of Eqs. (21)–(25) for constant mean input or small amplitude variations of it through a perturbative approach. It extends the technique proposed in [41] to the case of time-varying mean input within the ISI, and can be adjusted for small amplitude variations of other parameters in a straightforward way.

We consider $\mu_{\mathrm{ISI}}(s) = \mu^0_{\mathrm{ISI}} + J\mu^1_{\mathrm{ISI}}(s)$ with small $|J|$ according to Eq. (5). The solution of the first passage time system to first order in J can be expressed as $p_V(V, s) \approx p^0_V(V, s) + Jp^1_V(V, s)$. We insert this in the Fokker-Planck system and neglect terms of order > 1 in J. The resulting system is then Fourier-transformed over time using separation of variables, $p_V(V, s) = x(V)y(s)$, such that $\hat{p}_V(V; \omega) = \mathcal{F}[p_V(V, s)] = x(V)\hat{y}(\omega)$, with Fourier transform and the inverse transform defined by

$$\hat{y}(\omega) := \mathcal{F}[y(s)] = \int_{-\infty}^{\infty} y(s)e^{-\mathrm{i}\omega s} ds, \qquad y(s) = \mathcal{F}^{-1}[\hat{y}(\omega)] = \int_{-\infty}^{\infty} \frac{\hat{y}(\omega)}{2\pi} e^{\mathrm{i}\omega s} d\omega, \tag{27}$$

where ω denotes angular frequency. This yields the following two (coupled) systems, one for the steady-state solution $\hat{p}^0_V(V; \omega)$,

$$\frac{d\hat{q}^0_V}{dV} = -\mathrm{i}\omega\hat{p}^0_V \tag{28}$$

$$\frac{d\hat{p}^0_V}{dV} = \frac{2}{\sigma^2}\left([f(V) + \mu^0_{\mathrm{ISI}}]\,\hat{p}^0_V - \hat{q}^0_V\right) \tag{29}$$

subject to

$$\hat{p}^0_V(V_{\mathrm{s}}; \omega) = 0, \qquad \lim_{V \searrow -\infty} \hat{q}^0_V(V; \omega) = 0 \tag{30}$$

$$\lim_{V \searrow V_{\mathrm{r}}} \hat{q}^0_V(V; \omega) - \lim_{V \nearrow V_{\mathrm{r}}} \hat{q}^0_V(V; \omega) = 1 \tag{31}$$

and one for $\hat{p}^1_V(V; \omega)$,

$$\frac{d\hat{q}^1_V}{dV} = -\mathrm{i}\omega\hat{p}^1_V \tag{32}$$

$$\frac{d\hat{p}^1_V}{dV} = \frac{2}{\sigma^2}\left([f(V) + \mu^0_{\mathrm{ISI}}]\,\hat{p}^1_V + \hat{h}(V; \omega) - \hat{q}^1_V\right) \tag{33}$$

with function $\hat{h}(V; \omega) = \mathcal{F}[\mu^1_{\mathrm{ISI}}(s)p^0_V(V, s)]$, subject to

$$\hat{p}^1_V(V_{\mathrm{s}}; \omega) = 0, \qquad \lim_{V \searrow -\infty} \hat{q}^1_V(V; \omega) = 0. \tag{34}$$

The ISI density (in the frequency domain) is then given by

$$\hat{p}_{\mathrm{ISI}}(\omega) \approx \hat{p}^0_{\mathrm{ISI}}(\omega) + J\hat{p}^1_{\mathrm{ISI}}(\omega) = \hat{q}^0_V(V_{\mathrm{s}}; \omega) + J\hat{q}^1_V(V_{\mathrm{s}}; \omega). \tag{35}$$

We solve the linear ordinary differential equations (boundary value problems) (28)–(34) for each fixed frequency ω by splitting the solutions,

$$\hat{p}_V^0(V;\omega) = \hat{p}_{\mathrm{ISI}}^0(\omega)\hat{p}_\alpha^0(V;\omega) + \hat{p}_\beta^0(V;\omega), \qquad \hat{q}_V^0(V;\omega) = \hat{p}_{\mathrm{ISI}}^0(\omega)\hat{q}_\alpha^0(V;\omega) + \hat{q}_\beta^0(V;\omega) \tag{36}$$

and analogously for $\hat{p}_V^1(V;\omega)$, $\hat{q}_V^1(V;\omega)$. The components $(\hat{p}_\alpha^0, \hat{q}_\alpha^0)$ and $(\hat{p}_\beta^0, \hat{q}_\beta^0)$ respectively solve Eqs. (28)–(29) with $\hat{p}_\alpha^0 = 0$, $\hat{q}_\alpha^0 = 1$ and $\hat{p}_\beta^0 = \hat{q}_\beta^0 = 0$ at $V = V_\mathrm{s}$ and $\lim_{V\searrow V_\mathrm{r}} \hat{q}_\beta^0 - \lim_{V\nearrow V_\mathrm{r}} \hat{q}_\beta^0 = 1$. The components $(\hat{p}_\alpha^1, \hat{q}_\alpha^1)$ and $(\hat{p}_\beta^1, \hat{q}_\beta^1)$ solve Eqs. (32)–(33) with $\hat{p}_\alpha^1 = 0$, $\hat{q}_\alpha^1 = 1$ and $\hat{p}_\beta^1 = \hat{q}_\beta^1 = 0$ at $V = V_\mathrm{s}$. These solution components can be conveniently computed by backward integration from V_s to a sufficiently small lower bound $V_\mathrm{lb} < V_\mathrm{r}$. We then obtain $\hat{p}_{\mathrm{ISI}}^0$ and $\hat{p}_{\mathrm{ISI}}^1$ by satisfying the reflecting boundary conditions (in (30) and (34)):

$$\hat{p}_{\mathrm{ISI}}^0(\omega) = -\frac{\hat{q}_\beta^0(V_\mathrm{lb};\omega)}{\hat{q}_\alpha^0(V_\mathrm{lb};\omega)}, \qquad \hat{p}_{\mathrm{ISI}}^1(\omega) = -\frac{\hat{q}_\beta^1(V_\mathrm{lb};\omega)}{\hat{q}_\alpha^1(V_\mathrm{lb};\omega)}. \tag{37}$$

The ISI density (in the time domain) is finally calculated by the inverse transform, $p_{\mathrm{ISI}}(s|\mu_{\mathrm{ISI}}[0,s],\boldsymbol{\theta}) = \mathcal{F}^{-1}[\hat{p}_{\mathrm{ISI}}(\omega)]$ using Eqs. (35) and (37).

In practice, we first solve the steady-state system (28)–(31), evaluate the function $\hat{h}$ which appears in Eq. (33) and then solve the system for the change in ISI density due to the perturbation, (32)–(34). Note that knowledge of $\mu_{\mathrm{ISI}}^1(s)$ for $s \geq 0$ is required to calculate $\hat{h}$. If the input perturbations are given by delta pulses (as for the network in Results section 4) the calculation of $\hat{h}$ is greatly simplified; e.g., for a pulse at $s = s_0$, $\mu_{\mathrm{ISI}}^1(s) = \delta(s - s_0)$ we have $\hat{h}(V;\omega) = e^{-\mathrm{i}\omega s_0} p_V^0(V, s_0)$.

2.2 Method 1b: numerical solution based on finite volume discretization

This method employs a recently developed finite volume numerical scheme with implicit time discretization and Scharfetter-Gummel flux approximation, adapted from [42] for the first passage time problem. It provides an accurate solution of Eqs. (21)–(25) for arbitrary variations of the mean input. In brief, we first discretize the domain $[V_\mathrm{lb}, V_\mathrm{s}]$ into N_V equidistant grid cells $[V_{m-\frac{1}{2}}, V_{m+\frac{1}{2}}]$ with centers V_m, $m \in \{1,\dots,N_V\}$, $V_1 < V_2 < \cdots < V_{N_V}$, where $V_{\frac{1}{2}} = V_\mathrm{lb}$ and $V_{N_V+\frac{1}{2}} = V_\mathrm{s}$ are the out-most cell borders. Within each cell the numerical approximation of $p_V(V,s)$ is assumed to be constant and corresponds to the average value denoted by $p_V(V_m, s)$. Integrating Eq. (21) over the volume of cell m, and applying the divergence theorem, yields

$$\frac{\partial}{\partial s} p_V(V_m, s) = \frac{q_V(V_{m-\frac{1}{2}}, s) - q_V(V_{m+\frac{1}{2}}, s)}{\Delta V}, \tag{38}$$

where $\Delta V = V_2 - V_1$. To solve Eq. (38) forward in time (represented by the ISI variable s) the fluxes at the borders of each cell are approximated using the first order Scharfetter-Gummel flux [84],

$$q_V(V_{m+\frac{1}{2}}, s) = v_{m+\frac{1}{2}}(s)\, \frac{p_V(V_m, s) - p_V(V_{m+1}, s)\, \exp\left(-v_{m+\frac{1}{2}}(s)\Delta V/D\right)}{1 - \exp\left(-v_{m+\frac{1}{2}}(s)\Delta V/D\right)}, \tag{39}$$

where $v_{m+\frac{1}{2}}(s) = f(V_{m+\frac{1}{2}}) + \mu_{\mathrm{ISI}}(s)$ and $D = \frac{1}{2}\sigma^2$ denote the drift and diffusion coefficients, respectively.

For the time discretization we rewrite Eq. (38) (with Eq. (39)) in vectorized form and approximate the involved time derivative as first order backward difference to ensure numerical stability. This yields in each time step of length Δs a linear system for the vector $\mathbf{p}^{n+1}$ of probability density values at s_{n+1}, given the values $\mathbf{p}^n$ at the previous time step s_n, with vector elements $p_m^n = p_V(V_m, s_n)$,

$$(\mathbf{I} - \frac{\Delta s}{\Delta V}\, \mathbf{G}^n)\mathbf{p}^{n+1} = \mathbf{p}^n, \tag{40}$$

where $\mathbf{I}$ is the identity matrix and $\mathbf{G}^n \in \mathbb{R}^{N_V \times N_V}$ is a tridiagonal matrix that contains the discretization of the membrane voltage (cf. Eqs. (38), (39)), including the absorbing and reflecting boundary conditions (Eqs. (24) and (25)).

The ISI density, Eq. (26), in this representation is obtained by evaluating the flux, Eq. (39), at the spike voltage V_s, taking into account the absorbing boundary condition, Eq. (24), and introducing an auxiliary ghost cell [85] with center V_{N_V+1}, which yields

$$p_\mathrm{ISI}(s_{n+1}|\mu_\mathrm{ISI}[0,s_n],\boldsymbol{\theta}) = q_V(V_{N_V+\frac{1}{2}},s_{n+1}) = v_{N_V+\frac{1}{2}}(s_n)\,\frac{1+\exp(-v_{N_V+\frac{1}{2}}(s_n)\Delta V/D)}{1-\exp(-v_{N_V+\frac{1}{2}}(s_n)\Delta V/D)}\,p_{N_V}^{n+1}. \tag{41}$$

For additional details we refer to [42] (incl. supplemental material therein). Note that this method also allows for the variation of other parameters (in addition to the mean input) within the ISI. Naturally, the finite volume scheme can also be used as an alternative to the Fourier-based technique for computing p_ISI^0 and p_ISI^1 in method **1a** (using small amplitude variations of the mean input, cf. Eqs. (5) and (6)), which may be computationally more efficient in some cases; a comparison is provided at https://github.com/neuromethods/inference-for-integrate-and-fire-models.

3. Method 2: derived spike rate model

Method **2** requires the (instantaneous) spike rate $r(t)$ of the model neuron described by Eqs. (9) and (10), which can be calculated by solving a Fokker-Planck system similar to Eqs. (21)–(25):

$$\frac{\partial p_V}{\partial t}+\frac{\partial q_V}{\partial V}=0, \qquad q_V := [f(V)+\mu(t)]\,p_V - \frac{\sigma^2}{2}\frac{\partial p_V}{\partial V}, \qquad r(t)=q_V(V_\mathrm{s},t), \tag{42}$$

subject to the conditions

$$p_V(V_\mathrm{s},t)=0 \qquad \lim_{V\searrow-\infty} q_V(V,t)=0 \tag{43}$$

$$\lim_{V\searrow V_\mathrm{r}} q_V(V,t) - \lim_{V\nearrow V_\mathrm{r}} q_V(V,t) = q_V(V_\mathrm{s},t), \tag{44}$$

where Eq. (44) accounts for the reset condition (10). The steady-state solution of this system (for constant mean input) can be conveniently calculated [41]. To obtain the time-varying solution of Eqs. (42)–(44) is computationally more demanding and can be achieved, e.g., using a finite volume method as described in the previous section (see [42]).

As an efficient alternative reduced models have been developed which approximate the spike rate dynamics of this Fokker-Planck system by a low-dimensional ODE that can be solved much faster [42–44, 86]. Here we employ a simple yet accurate reduced model from [42] (the LNexp model, based on [43]) adapted for leaky I&F neurons with constant input variance σ^2. This model is derived via a linear-nonlinear cascade ansatz, where the mean input is first linearly filtered and then passed though a nonlinear function to yield the spike rate. Both components are determined from the Fokker-Planck system and can be conveniently calculated without having to solve Eqs. (42)–(44) forward in time: the linear temporal filter is obtained from the first order spike rate response to small amplitude modulations of the mean input and the nonlinearity is obtained from the steady-state solution [42, 43]. The filter is approximated by an exponential function and adapted to the input in order to allow for large deviations of μ. This yields a one-dimensional ODE for the filter application,

$$\frac{d\mu_\mathrm{f}}{dt}=\frac{\mu(t)-\mu_\mathrm{f}}{\tau_\mu(\mu_\mathrm{f})}, \tag{45}$$

where μ_f is the filtered mean input and τ_μ is the (state dependent) time constant. The spike rate is given by the steady-state spike rate of the Fokker-Planck system evaluated at $\mu=\mu_\mathrm{f}$,

$$r(t)=r_\infty(\mu_\mathrm{f}). \tag{46}$$

In order to efficiently simulate this model we pre-calculate τ_μ and r_∞ for a reasonable range of mean input values and use look-up tables during time integration. We would like to remark that this model is based on the derivation in [43] with filter approximation scheme proposed in [42] which leads to improved accuracy of spike rate reproduction for the sensitive low input regime [42]. For a given mean input time series $\mu[t_0,t]$ we calculate $r(t|\mu[t_0,t],\boldsymbol{\theta})$ using the initial condition $\mu_\mathrm{f}(t_0)=\mu(t_0)$.

4. Likelihood maximization

We maximized the logarithm of the likelihood (log-likelihood),

$$\mathrm{argmax}_{\boldsymbol{\theta}}\, \log p(\mathrm{D}|\boldsymbol{\theta}) = \mathrm{argmax}_{\boldsymbol{\theta}} \sum_{k=1}^{K-1} \log p(t_{k+1}|t_k, \mu[t_k, t_{k+1}], \boldsymbol{\theta}) \tag{47}$$

for individual neurons (where we have used Eq. (3)) and similarly for networks (using the logarithm in Eq. (8)). Optimization was performed using a simplex algorithm [87] as implemented in the Scipy package for Python. It should be noted that our method is not restricted to this algorithm, other (e.g., gradient-based) optimization techniques may also be applied.

5. Fisher information per ISI

To quantify how well the parameters can be estimated we calculate the Fisher information per ISI for parameter θ (component of $\boldsymbol{\theta}$) defined by

$$\mathcal{I}(\theta) := \int_0^\infty \left(\frac{\partial}{\partial \theta} \log\Big(p_{\mathrm{ISI}}(s|\mu[0,s],\theta)\Big)\right)^2 p_{\mathrm{ISI}}(s|\mu[0,s],\theta)\, ds. \tag{48}$$

In case of a single (non-adapting) model neuron with constant input moments the Fisher information for spike trains with K spikes is given by $(K-1)\,\mathcal{I}(\theta)$ due to additivity. In this case we can analytically calculate the Cramer-Rao bound by $[(K-1)\,\mathcal{I}(\theta)]^{-1}$, which limits the variance of any unbiased estimator of θ from below. A maximum likelihood estimator is known to achieve this bound as the sample size grows large (i.e., $K \to \infty$).

6. Detection of input perturbations

We quantified the sensitivity to detect weak input perturbations using our estimation methods (**1a** and **2**) in comparison with a detection method based on the generated data only. For a given parametrization N_{r} spike trains were simulated using different realizations of neuronal input noise and perturbation onset (trigger) times. Detection sensitivity based on the estimation methods was assessed by the fraction of $N_{\mathrm{r}} = 50$ estimates of J for true $J > 0$ ($J < 0$) that exceeded the 95 %-ile (fell below the 5 %-ile) of estimates without perturbation (i.e., $J = 0$).

The data-driven reference method was based on CCGs between the spike trains and perturbation times (in other words, spike density curves aligned to perturbation onset times). For each of $N_{\mathrm{r}} = 300$ realizations one such curve was calculated by the differences between spike times and the perturbation onset times using a Gaussian kernel with 3 ms standard deviation (kernel density estimation). Detection sensitivity was assessed by the fraction of spike density curves for which a significant peak (for $J > 0$) or trough (for $J < 0$) appeared in the interval [0, 100 ms]. Significance was achieved for true $J > 0$ ($J < 0$) if the curve maximum (minimum) exceeded the 95 %-ile (fell below the 5 %-ile) of maxima (minima) without perturbation in that interval.

7. Fitting I&F neurons to spike trains from electrophysiological recordings

7.1 Estimation of neuronal input statistics using in-vitro ground truth data

We used somatic whole-cell current clamp recordings from primary somatosensory cortex in acute brain slices (for details see [34]). Layer 5 PYRs were recorded in wild-type mice [34], fast-spiking layer 5 INTs were selected among the fluorescing cells of a GAD67-GFP transgenic line [88]. Only cells with an access resistance $\leq$25 MΩ (PYR: 18.3±1.5 MΩ, n = 7; INT: 19.5±4.0 MΩ, n = 6) and a drift in the resting membrane potential $\leq$7.5 mV (PYR: 3.2±3.0 mV, n = 7; INT: 3.1±3.7 mV, n = 6) throughout the recording were retained for further analysis. Seven PYRs and six INTs were stimulated with a fluctuating current $I(t)$ generated

according to an Ornstein-Uhlenbeck process,

$$\frac{dI}{dt} = \frac{\mu_I - I}{\tau_I} + \sqrt{\frac{2}{\tau_I}}\sigma_I \xi(t), \tag{49}$$

where τ_I denotes the correlation time, μ_I and σ_I are the mean and standard deviation of the stationary normal distribution, i.e., $\lim_{t\to\infty} I(t) \sim \mathcal{N}(\mu_I, \sigma_I^2)$, and ξ is a unit Gaussian white noise process. Somatic current injections lasted 5 s and were separated by inter-stimulus intervals of at least 25 s. Different values for μ_I and σ_I were used and each combination was repeated three times. The correlation time was set to 3 ms. Spike times were defined by the time at which the membrane voltage crossed 0 mV from below, which was consistent with a large depolarization rate $dV/dt > 10$ mV/ms [34]. An absolute refractory period of 3 ms was assumed.

For each neuron we fitted a leaky I&F model with and without adaptation (cf. Methods sections 1.1 and 1.4). Note that the injected current $I(t)$ can be well approximated by a Gaussian white noise process as considered in our model because of the small correlation time τ_I. In Results section 2 we estimated the input parameters μ and σ for nonadaptive model neurons from each 5 s-long spike train recording as well as from each combined 3×5 s-long recording (using the three repetitions with identical stimulus parameters which effectively yielded 15 s long stimuli). To exclude onset transients (i.e., increased spike rate upon stimulus onset) we used the central 90% of ISIs for each stimulus, ensuring that ISIs lasted > 5 ms. In Results section 5 we additionally estimated the adaptation parameters Δw and τ_w per neuron across all available stimuli in the combined 15 s stimulus setting. Here we used all ISIs (including the short ones at stimulus onset) in order to unmask adaptation effects. Parameter estimation was accomplished using methods **1a** and **1b**. To compare the quality of the two models and avoid over-fitting we used the Akaike information criterion (AIC, [36, 89]), given by $2N_{\boldsymbol{\theta}} - \max_{\boldsymbol{\theta}} \log p(\mathrm{D}|\boldsymbol{\theta})$, where $N_{\boldsymbol{\theta}}$ denotes the number of estimated parameters for a particular model. The preferred model from a set of candidate models is the one with the smallest AIC value.

7.2 Estimation of synaptic connections using in-vivo ground truth data

We used combined juxtacellular-extracellular recordings of neuronal ensembles from the hippocampal CA1 region in awake mice (for details see [35]). Neurons were separated into PYRs and INTs according to their spiking statistics. Spikes were evoked in single PYRs by short current pulses (50-100 ms) applied at intervals of variable length using juxtacellular electrodes while recording extracellular spikes of local INTs. PYR spikes which occurred during a stimulus were considered as evoked, and those which occurred at all other times were considered as spontaneous. All spikes that occurred during sharp-wave ripple events were discarded from the analyses, and we only considered INTs that fired at least 3 spikes/s on average. A total of 78 PYR-INT pairs were included for estimation of synaptic couplings.

For each INT we considered a leaky I&F neuron receiving background input and (potential) synaptic input from the recorded PYR such that each presynaptic spike causes a delayed (with delay d) postsynaptic potential of size J:

$$\frac{dV}{dt} = -\frac{V}{\tau_\mathrm{m}} + \mu(t) + J\sum_{k=1}^{K}\delta(t - t_k - d) + \sigma\xi(t) \tag{50}$$

$$\text{if } V(t) \geq V_\mathrm{s} \text{ then } V(t) \leftarrow V_\mathrm{r}, \tag{51}$$

where t_k denotes the k-th spike time of K PYR spikes (cf. Methods section 1.4). To account for changes in background input statistics over the recording duration (which lasted up to ∼2h) and to reflect low-frequency network co-modulation induced by common network drive the background mean input was allowed to vary over time. The parameters to be estimated are thus $\mu(t)$, J, d and σ. Estimation consisted of three steps. First, we inferred the statistics $\mu(t)$ and σ of background inputs (described by a non-stationary stochastic process) for $J = 0$ in the following way. We computed the empirical instantaneous spike rate $r(t)$ of the INT from the observed spike train via kernel density estimation using a Gaussian kernel with width $\sigma_\mathrm{G} \in \{0.1, 0.5, 1\}$ s. The estimated empirical spike rate varies over time much slower than the timescale at which changes of mean input translate to changes of spike rate in the I&F model. This justifies the approximation $r(t) \approx r_\infty(\mu(t))$

(cf. methods section 3), which allowed us to efficiently evaluate the spike train likelihood for fixed σ by applying method **1a** with mean input assumed constant within each ISI, given by $\mu(t) = r_\infty^{-1}(r(t))$ (at the center between consecutive spike times). The likelihood was then maximized with respect to σ. Given the parameters for the background inputs (one value of μ per ISI and one for σ) we next maximized the likelihood of the (full) model in the second step with respect to J and d using method **1a**. In the third step we assessed the significance of synaptic coupling estimates using pseudo data. We perturbed the presynaptic spike times by a small temporal jitter (random values between -5 and +5 ms) and (re-)estimated J and d. This was repeated 100 times and z-scores were computed from the estimated coupling strengths. Notably, since spike times are shifted by only small values, effects due to network co-modulation (which occurs on a slower timescale) are preserved in the pseudo data. In this way we obtained a coupling strength z-score for each PYR-INT pair and for each of the three values of σ_G. In addition, we combined these results and computed a "combined timescale" estimate as the largest absolute z-score across the three timescales (σ_G values) for each connection.

We validated our results against ground-truth data obtained from juxtacellular evoked activity using a model-free method based on spike train CCGs [35]. (Mono)synaptic connections were assumed to produce excess synchrony above baseline co-modulation in a short interval following PYR spikes. To generate estimated ground truth connection labels a CCG (0.4 ms binning) was computed for each PYR-INT pair using the evoked PYR spikes. For positive labels the peak of the CCG in the interval $[0.8, 2.8]$ ms needed to exceed that from the slowly co-modulated baseline, and it needed to be significantly larger than the largest peak in the anticausal direction (short negative lags). The lower frequency baseline was computed by convolving the observed CCG with a "partially hollow" Gaussian kernel, with a standard deviation of 10 ms and a hollow fraction of 60%. We estimated the probability of obtaining a spike count sc of n as observed (or higher) in the m^{th} time lag within $[0.8, 2.8]$ ms of the CCG, given the expected, low frequency baseline rate $\lambda_\mathrm{s}(m)$ using the Poisson distribution with a continuity correction,

$$P_\mathrm{fast}(sc(m) \geq n|\lambda_\mathrm{s}(m)) = 1 - \sum_{k=0}^{n-1} \frac{\lambda_\mathrm{s}^k(m) e^{-\lambda_\mathrm{s}(m)}}{k!} - \frac{\lambda_\mathrm{s}^n(m) e^{-\lambda_\mathrm{s}(m)}}{n!\,2}. \tag{52}$$

Similarly, we estimated the probability of obtaining the observed spike count n (or higher) in the m^{th} time lag within $[0.8, 2.8]$ ms of the CCG as expected from the maximum rate λ_a across negative lags within $[-2, 0]$ ms using the Poisson distribution with a continuity correction,

$$P_\mathrm{causal}(sc(m) \geq n|\lambda_\mathrm{a}) = 1 - \sum_{k=0}^{n-1} \frac{\lambda_\mathrm{a}^k e^{-\lambda_\mathrm{a}}}{k!} - \frac{\lambda_\mathrm{a}^n e^{-\lambda_\mathrm{a}}}{n!\,2}. \tag{53}$$

Connections were labeled as synapses if $P_\mathrm{fast} < 0.001$ and $P_\mathrm{causal} < 0.0026$ for all (binned) lags in $[0.8, 2.8]$ ms, according to the rigorous criterion defined in [35].

Based on these labels we computed ROC curves as well as ACC and BACC (cf. methods section 1.4) using a classification (z-score) threshold value J^z_thresh. Accordingly, the presence of an estimated connection was assured by the condition $\hat{J}^z > J^z_\mathrm{thresh}$, where $\hat{J}^z$ denotes the connection strength (z-score) estimate for a given PYR-INT pair. Note, that the ground truth labels indicate positive excitatory connections (positives) and absent connections (negatives).

To test the validity of our approach we estimated connectivity using only the first evoked PYR spikes of each stimulation pulse (which are maximally decoupled from network co-modulation) and compared the results with the ground truth labels. This assessment yielded excellent agreement, with ACC and BACC values of up to 0.97 and 0.95, respectively (for $\sigma_\mathrm{G} = 0.1$ s).

7.3 Estimation of hidden neuronal inputs using data from awake animals

We further used single unit spike trains from extracellular recordings of two adult female ferrets in different behavioral conditions. The animals were either passively listening or actively discriminating click trains of different rates. Each stimulus trial contained a period of silence lasting 0.4 s and a periodic click train (with

sound level 70 dB SPL) over a duration of 0.75 s. Neural activity from primary auditory cortex was recorded using a 24 channel electrode and spike sorted using an automatic clustering algorithm followed by a manual adjustment of the clusters (for details see [53]: click rate discrimination task with spike sorting performed on the pre-passive and active sessions). Spike trains with > 50 ISIs during silence periods were considered for model fitting. 71 single units (out of 82 in total) passed that threshold in each of the two behavioral conditions.

Model neurons were fit in either behavioral condition separately (resulting in 142 sets of estimated parameters). We employed the leaky I&F model (Eqs. (9), (10)) with $\mu(t) = \mu_0 + J_\mathrm{e}\mu_\mathrm{e}(t) + J_\mathrm{i}\mu_\mathrm{i}(t)$, $J_\mathrm{e} \geq 0$, $J_\mathrm{i} \leq 0$, where $\mu_\mathrm{e}(t)$, $\mu_\mathrm{i}(t)$ are given by the superposition of alpha functions with time constants τ_e, τ_i, respectively, triggered at the click times (cf. Eq. (13)). The parameters of the background input (μ_0 and σ) were first estimated from baseline spike train data using method **1a** with $J_\mathrm{e} = J_\mathrm{i} = 0$. For robust estimation we used the central 95% of ISIs, ensuring that ISIs lasted > 2.5 ms. The parameters of the click-triggered inputs (J_e, τ_e, J_i and τ_i) were then estimated from the data during click train periods using method **2**, where we omitted the first click to exclude transients related to the noise stimulus that immediately preceded the click period. Specifically, we minimized $-\log p(\mathrm{D}|\boldsymbol{\theta}) + J_\mathrm{e}^2 + J_\mathrm{i}^2$, i.e., the negative log-likelihood plus a quadratic regularization term to prevent solutions with large excitatory and inhibitory inputs that cancel each other. Beforehand we re-estimated μ_0 from baseline data using method **2** (with pre-determined σ) to avoid a potential bias caused by the switch between estimation methods. Method **2** was used instead of method **1** in order to correctly estimate potentially strong click-triggered inputs in a computationally efficient way.

For comparison we considered three simpler models: a Poisson process with constant rate for the baseline setting, an I&F model with constant mean input $\mu(t) = \mu_0 + \Delta\mu$ for the click periods, and an I&F model with mean input $\mu(t) = \mu_0 + J\mu_1(t)$, where $\mu_1(t)$ is given by the superposition of alpha functions with time constant τ and latency d, triggered at the click times (i.e., using Eq. (13) with click time $\tilde{t}_l$ replaced by $\tilde{t}_l - d$). Parameter estimation for these models was performed using method **2** (without regularization). To compare the quality of the models we used the AIC.

Acknowledgments

This work was supported by Deutsche Forschungsgemeinschaft in the framework of Collaborative Research Center 910, the Programme Emergences of the City of Paris, ANR project MORSE (ANR-16-CE37-0016), and the program "Investissements d'Avenir" launched by the French Government and implemented by the ANR, with the references ANR-10-LABX-0087 IEC and ANR-11-IDEX-0001-02 PSL* Research University. The funders had no role in study design, data collection and analysis, decision to publish, or preparation of the manuscript.

References

1. Chichilnisky EJ. A simple white noise analysis of neuronal light responses. Network. 2001;12:199–213.

2. Truccolo W, Eden UT, Fellows MR, Donoghue JP, Brown EN. A Point Process Framework for Relating Neural Spiking Activity to Spiking History, Neural Ensemble, and Extrinsic Covariate Effects. J Neurophysiol. 2005;93:1074–1089.

3. Pillow JW, Shlens J, Paninski L, Sher A, Litke AM, Chichilnisky EJ, et al. Spatio-temporal correlations and visual signalling in a complete neuronal population. Nature. 2008;454:995–999.

4. Latimer KW, Yates JL, Meister MLR, Huk AC, Pillow JW. Single-trial spike trains in parietal cortex reveal discrete steps during decision-making. Science. 2015;349:184–187.

5. Aljadeff J, Lansdell BJ, Fairhall AL, Kleinfeld D. Analysis of Neuronal Spike Trains, Deconstructed. Neuron. 2016;91:221–259.

6. Jolivet R, Schürmann F, Berger TK, Naud R, Gerstner W, Roth A. The quantitative single-neuron modeling competition. Biol Cybern. 2008;99:417–426.

7. Badel L, Lefort S, Brette R, Petersen CCH, Gerstner W, Richardson MJE. Dynamic I-V curves are reliable predictors of naturalistic pyramidal-neuron voltage traces. J Neurophysiol. 2008;99:656–666.

8. Gerstner W, Naud R. How Good Are Neuron Models? Science. 2009;326:379–380.

9. Brette R, Gerstner W. Adaptive exponential integrate-and-fire model as an effective description of neuronal activity. J Neurophysiol. 2005;94:3637–3642.

10. Pospischil M, Piwkowska Z, Bal T, Destexhe A. Comparison of different neuron models to conductance-based post-stimulus time histograms obtained in cortical pyramidal cells using dynamic-clamp in vitro. Biol Cybern. 2011;105:167–180.

11. Harrison PM, Badel L, Wall MJ, Richardson MJE. Experimentally Verified Parameter Sets for Modelling Heterogeneous Neocortical Pyramidal-Cell Populations. PLOS Comput Biol. 2015;11:1–23.

12. Pozzorini C, Mensi S, Hagens O, Naud R, Koch C, Gerstner W. Automated High-Throughput Characterization of Single Neurons by Means of Simplified Spiking Models. PLOS Comput Biol. 2015;11:e1004275.

13. de Solages C, Szapiro G, Brunel N, Hakim V, Isope P, Buisseret P, et al. High-Frequency Organization and Synchrony of Activity in the Purkinje Cell Layer of the Cerebellum. Neuron. 2008;58:775–788.

14. Giridhar S, Doiron B, Urban NN. Timescale-dependent shaping of correlation by olfactory bulb lateral inhibition. Proc Natl Acad Sci USA. 2011;108:5843–5848.

15. Litwin-Kumar A, Chacron MJ, Doiron B. The Spatial Structure of Stimuli Shapes the Timescale of Correlations in Population Spiking Activity. PLOS Comput Biol. 2012;8:e1002667.

16. Potjans TC, Diesmann M. The cell-type specific cortical microcircuit: Relating structure and activity in a full-scale spiking network model. Cerebral Cortex. 2014;24:785–806.

17. Bendor D. The role of inhibition in a computational model of an auditory cortical neuron during the encoding of temporal information. PLOS Comput Biol. 2015;11:e1004197.

18. Blot A, de Solages C, Ostojic S, Szapiro G, Hakim V, Léna C. Time-invariant feed-forward inhibition of Purkinje cells in the cerebellar cortex in vivo. The Journal of physiology. 2016;10:2729–2749.

19. Kanashiro T, Ocker GK, Cohen MR, Doiron B. Attentional modulation of neuronal variability in circuit models of cortex. eLife. 2017;6:1–38.

20. Brunel N, Hakim V. Fast global oscillations in networks of integrate-and-fire neurons with low firing rates. Neural Comput. 1999;11:1621–1671.

21. Brunel N. Dynamics of sparsely connected networks of excitatory and inhibitory spiking neurons. J Comput Neurosci. 2000;8:183–208.

22. Izhikevich EM, Edelman G. Large-scale model of mammalian thalamocortical systems. Proc Natl Acad Sci USA. 2008;105:3593–3598.

23. Litwin-Kumar A, Doiron B. Slow dynamics and high variability in balanced cortical networks with clustered connections. Nat Neurosci. 2012;15:1498–1505.

24. Doiron B, Litwin-Kumar A, Rosenbaum R, Ocker GK, Josić K. The mechanics of state-dependent neural correlations. Nat Neurosci. 2016;19:383–393.

25. Brüderle D, Petrovici MA, Vogginger B, Ehrlich M, Pfeil T, Millner S, et al. A comprehensive workflow for general-purpose neural modeling with highly configurable neuromorphic hardware systems. Biol Cybern. 2011;104:263–296.

26. Pfeil T, Grübl A, Jeltsch S, Müller E, Müller P, Petrovici MA, et al. Six networks on a universal neuromorphic computing substrate. Front Neurosci. 2013;7:1–17.

27. Schmuker M, Pfeil T, Nawrot MP. A neuromorphic network for generic multivariate data classification. Proc Natl Acad Sci USA. 2014;111:2081–2086.

28. Paninski L, Pillow JW, Simoncelli EP. Maximum Likelihood Estimation of a Stochastic Integrate-and-Fire Neural Encoding Model. Neural Comput. 2004;16:2533–2561.

29. Hawrylycz M, Anastassiou C, Arkhipov A, Berg J, Buice M, Cain N, et al. Inferring cortical function in the mouse visual system through large-scale systems neuroscience. Proc Natl Acad Sci USA. 2016;113:7337–7344.

30. Gerstner W, Kistler WM, Naud R, Paninski L. Neuronal Dynamics: From Single Neurons to Networks and Models of Cognition. Cambridge, UK: Cambridge University Press; 2014.

31. Druckmann S, Banitt Y, Gidon A, Schürmann F, Markram H, Segev I. A novel multiple objective optimization framework for constraining conductance-based neuron models by experimental data. Front Neurosci. 2007;1:7–18.

32. Rossant C, Goodman DFM, Fontaine B, Platkiewicz J, Magnusson AK, Brette R. Fitting neuron models to spike trains. Front Neurosci. 2011;5:1–8.

33. Stringer C, Pachitariu M, Steinmetz NA, Okun M, Bartho P, Harris KD, et al. Inhibitory control of correlated intrinsic variability in cortical networks. eLife. 2016;5:1–33.

34. Mensi S, Hagens O, Gerstner W, Pozzorini C. Enhanced Sensitivity to Rapid Input Fluctuations by Nonlinear Threshold Dynamics in Neocortical Pyramidal Neurons. PLOS Comput Biol. 2016;12:e1004761.

35. English DF, McKenzie S, Evans T, Kim K, Yoon E, Buzsáki G. Pyramidal Cell-Interneuron Circuit Architecture and Dynamics in Hippocampal Networks. Neuron. 2017;96:505–520.

36. Millar RB. Maximum Likelihood Estimation and Inference. Wiley; 2011.

37. Brunel N, Van Rossum MCW. Lapicque's 1907 paper: From frogs to integrate-and-fire. Biol Cybern. 2007;97:337–339.

38. Fourcaud-Trocmé N, Hansel D, van Vreeswijk C, Brunel N. How spike generation mechanisms determine the neuronal response to fluctuating inputs. J Neurosci. 2003;23:11628–11640.

39. Gigante G, Mattia M, Giudice P, Del Giudice P. Diverse population-bursting modes of adapting spiking neurons. Phys Rev Lett. 2007;98:148101.

40. Ladenbauer J, Augustin M, Obermayer K. How adaptation currents change threshold, gain and variability of neuronal spiking. J Neurophysiol. 2014;111:939–953.

41. Richardson MJE. Spike-train spectra and network response functions for non-linear integrate-and-fire neurons. Biol Cybern. 2008;99:381–92.

42. Augustin M, Ladenbauer J, Baumann F, Obermayer K. Low-dimensional spike rate models derived from networks of adaptive integrate-and-fire neurons: comparison and implementation. PLOS Comput Biol. 2017;13:e1005545.

43. Ostojic S, Brunel N. From spiking neuron models to linear-nonlinear models. PLOS Comput Biol. 2011;7:e1001056.

44. Mattia M, Del Giudice P. Population dynamics of interacting spiking neurons. Phys Rev E. 2002;66:051917.

45. Burkitt AN. A review of the integrate-and-fire neuron model: I. Homogeneous synaptic input. Biol Cybern. 2006;95:1–19.

46. Tuckwell HC. Introduction to Theoretical Neurobiology. Cambridge, UK: Cambridge University Press; 1988.

47. Ecker AS, Berens P, Keliris GA, Bethge M, Logothetis NK, Tolias AS. Decorrelated neuronal firing in coritcal micorcircuits. Science. 2010;327:584–587.

48. Cohen MR, Kohn A. Measuring and interpreting neuronal correlations. Nat Neurosci. 2011;14:811–819.

49. Madison DV, Nicoll RA. Control of the repetitive discharge of rat CA1 pyramidal neurones in vitro. J Physiol. 1984;354:319–331.

50. Schwindt PC, Spain WJ, Foehring RC, Chubb MC, Crill WE. Slow conductances in neurons from cat sensorimotor cortex in vitro and their role in slow excitability changes. J Neurophysiol. 1988;59:450–467.

51. Stocker M. Ca(2+)-activated K+ channels: molecular determinants and function of the SK family. Nat Rev Neurosci. 2004;5:758–770.

52. La Camera G, Rauch A, Thurbon D, Lüscher HR, Senn W, Fusi S. Multiple time scales of temporal response in pyramidal and fast spiking cortical neurons. J Neurophysiol. 2006;96:3448–3464.

53. Bagur S, Averseng M, Elgueda D, David S, Fritz J, Yin P, et al. Task Engagement Enhances Population Encoding of Stimulus Meaning in Primary Auditory Cortex 2. bioRxiv preprint. 2017; p. 1–51.

54. Wehr M, Zador AM. Balanced inhibition underlies tuning and sharpens spike timing in auditory cortex. Nature. 2003;426:442–446.

55. Wehr M, Zador AM. Synaptic mechanisms of forward suppression in rat auditory cortex. Neuron. 2005;47:437–445.

56. Xue M, Atallah BV, Scanziani M. Equalizing excitation-inhibition ratios across visual cortical neurons. Nature. 2014;511:596–600.

57. Oliphant TE. Python for Scientific Computing. Comput Sci Eng. 2007;9:10–20.

58. Lam SK, Pitrou A, Seibert S. Numba: A LLVM-based python JIT compiler. In: Proc. LLVM Compil. Infrastruct. HPC; 2015. p. 1–6.

59. Dong Y, Mihalas S, Russell A, Etienne-Cummings R, Niebur E. Estimating Parameters of Generalized Integrate-and-Fire Neurons from the Maximum Likelihood of Spike Trains. Neural Comput. 2011;23:2833–2867.

60. Mullowney P, Iyengar S. Parameter estimation for a leaky integrate-and-fire neuronal model from ISI data. J Comput Neurosci. 2008;24:179–194.

61. Kim H, Shinomoto S. Estimating nonstationary input signals from a single neuronal spike train. Phys Rev E. 2012;86:1–12.

62. Carlson KD, Nageswaran JM, Dutt N, Krichmar JL. An efficient automated parameter tuning framework for spiking neural networks. Front Neurosci. 2014;8:1–15.

63. Lueckmann JM, Goncalves PJ, Bassetto G, Öcal K, Nonnenmacher M, Macke JH. Flexible statistical inference for mechanistic models of neural dynamics. In: Advances in Neural Information Processing Systems; 2017. p. 1–18.

64. Cocco S, Leibler S, Monasson R. Neuronal couplings between retinal ganglion cells inferred by efficient inverse statistical physics methods. Proc Natl Acad Sci USA. 2009;106:14058–14062.

65. Monasson R, Cocco S. Fast inference of interactions in assemblies of stochastic integrate-and-fire neurons from spike recordings. J Comput Neurosci. 2011;31:199–227.

66. Zaytsev YV, Morrison A, Deger M. Reconstruction of recurrent synaptic connectivity of thousands of neurons from simulated spiking activity. J Comput Neurosci. 2015;39:77–103.

67. Pernice V, Rotter S. Reconstruction of sparse connectivity in neural networks from spike train covariances. J Stat Mech. 2013;3.

68. Casadiego J, Maoutsa D, Timme M. Inferring network connectivity from event timing patterns. arXiv preprint. 2018;.

69. Ostojic S, Brunel N, Hakim V. How connectivity, background activity, and synaptic properties shape the cross-correlation between spike trains. J Neurosci. 2009;29:10234–53.

70. Pernice V, Staude B, Cardanobile S, Rotter S. How structure determines correlations in neuronal networks. PLOS Comput Biol. 2011;7:e1002059.

71. Trousdale J, Hu Y, Shea-Brown E, Josi?? K. Impact of network structure and cellular response on spike time correlations. PLOS Comput Biol. 2012;8.

72. Rosenbaum R, Smith MA, Kohn A, Rubin JE, Doiron B. The spatial structure of correlated neuronal variability. Nat Neurosci. 2017;20:107–114.

73. Ocker GK, Josić K, Shea-Brown E, Buice MA. Linking structure and activity in nonlinear spiking networks. PLOS Comput Biol. 2017;13:e1005583.

74. Ocker GK, Hu Y, Buice MA, Doiron B, Josić K, Rosenbaum R, et al. From the statistics of connectivity to the statistics of spike times in neuronal networks. Curr Opin Neurobiol. 2017;46:109–119.

75. Vidne M, Ahmadian Y, Shlens J, Pillow JW, Kulkarni J, Litke AM, et al. Modeling the impact of common noise inputs on the network activity of retinal ganglion cells. J Comput Neurosci. 2012;33:97–121.

76. Brinkman BAW, Rieke F, Shea-Brown E, Buice MA. Predicting how and when hidden neurons skew measured synaptic interactions. bioRxiv preprint. 2017; p. 1–50.

77. Richardson M. Effects of synaptic conductance on the voltage distribution and firing rate of spiking neurons. Phys Rev E. 2004;69:051918.

78. Ghanbari A, Malyshev A, Volgushev M, Stevenson IH. Estimating short-term synaptic plasticity from pre- and postsynaptic spiking. PLOS Comput Biol. 2017;13:e1005738.

79. Stevenson I, Koerding K. Inferring spike-timing-dependent plasticity from spike train data. In: Advances in Neural Information Processing Systems; 2011. p. 1–9.

80. Linderman SW, Stock CH, Adams RP. A Framework for Studying Synaptic Placticity with Neural Spike Train Data. In: Advances in Neural Information Processing Systems; 2014. p. 1–9.

81. Stimberg M, Goodman DFM, Benichoux V, Brette R. Equation-oriented specification of neural models for simulations. Front Neuroinform. 2014;8:1–14.

82. Risken H. The Fokker-Planck Equation: Methods of Solutions and Applications. Berlin: Springer; 1996.

83. Ostojic S. Inter-spike interval distributions of spiking neurons driven by fluctuating inputs. J Neurophysiol. 2011;106:361–373.

84. Gosse L. Computing qualitatively correct approximations of balance laws. vol. 2. Springer; 2013.

85. LeVeque RJ. Finite volume methods for hyperbolic problems. Cambridge University Press; 2002.

86. Schaffer ES, Ostojic S, Abbott LF. A complex-valued firing-rate model that approximates the dynamics of spiking networks. PLOS Comput Biol. 2013;9:e1003301.

87. Nelder JA, Mead R. A Simplex Method for Function Minimization. Comput J. 1965;7:308–313.

88. Tamamaki N, Yanagawa Y, Tomioka R, Miyazaki JI, Obata K, Kaneko T. Green Fluorescent Protein Expression and Colocalization with Calretinin, Parvalbumin, and Somatostatin in the GAD67-GFP Knock-In Mouse. J Comp Neurol. 2003;467:60–79.

89. Akaike H. A New Look at the Statistical Model Identification. IEEE Trans Autom Control. 1974;19:716–723.